Title

Rotary Inchworm Motor for Underwater Microrobot Propulsion

Permalink

https://escholarship.org/uc/item/6vf3v1s8

Author

Bustamante Eguiguren, Mauricio Jose

Publication Date

2024

Peer reviewed|Thesis/dissertation

Rotary Inchworm Motor for Underwater Microrobot Propulsion

by

Mauricio J. Bustamante Eguiguren

A dissertation submitted in partial satisfaction of the

requirements for the degree of

Doctor of Philosophy

in

Engineering - Electrical Engineering and Computer Sciences

in the

Graduate Division

of the

University of California, Berkeley

Committee in charge:

Professor Michel Maharbiz, Co-chair
Professor Kristofer S.J.Pister, Co-chair
Professor Dorian Liepmann

Summer 2024

Rotary Inchworm Motor for Underwater Microrobot Propulsion

Abstract

Rotary Inchworm Motor for Underwater Microrobot Propulsion

by

Mauricio J. Bustamante Eguiguren

Doctor of Philosophy in Engineering - Electrical Engineering and Computer Sciences

University of California, Berkeley

Professor Michel Maharbiz, Co-chair

Professor Kristofer S.J.Pister, Co-chair

Swimming microrobots have significant potential for biomedical applications and distributed sensing. To date, most work has relied on external fields for control control. To achieve autonomy, locally controllable propulsion mechanisms must be developed. This thesis presents an rotary inchworm motor designed to drive an artificial flagellum, inspired by bacterial flagellar motors found in nature. The design adapts electrostatic gap closing actuators with angled arms for rotational motion. The devices are fabricated in an SOI process with a bonded lid featuring through-wafer vias as a mechanical feedthrough for the flagellum. A hydrophobic coating is applied to prevent water ingress through small gaps, thus keeping the gap closing actuators dry. This process also provides an additional layer of routing for reduced complexity. Motors with rotation rates up to 633 rpm at actuation frequencies of 1.7 kHz are demonstrated to operate reliably in dry conditions. Additionally, promising electrical and optical results are presented, preventing water ingress to gap-closing actuators at low pressures. Effective operation of the mechanism underwater remains a challenge.

A mi hermana, Sofía

Contents

List of Figures

List of Tables

Acknowledgments

The work compiled in this dissertation, and all the work that led to negative results and is not included, would not have been possible without the support of faculty, staff, friends, and family. Completing the PhD was difficult in ways I could not have expected– the support network I had going in and I have been furtunate to construct in my time at Berkeley is the most precious thing a person can have.

I'd like to begin by thanking Michel Maharbiz. I came to Berkeley to work with Michel and, despite its risks, thouroughly enjoyed embarking in crazy projects with high likelyhood of failure. I'd also like to thank Kris Pister, who took me in as an advisee and provided support and advice. I hope to learn something about the way both of you coduct your lives.

In addition, Dorian Liepmann graciously served in my dissertation and Qualification Exam comittee and provided technical fluid dyanmics knowledge that was key to the work contained in this disseratation. In addition, Ming Wu was the chair of my Qualification Exam committee; I will never forget his calming demeanor during times of inmense stress.

The devices in this work were fabricated in the Marvell Nanotechnlogy Laboratory, whose staff was a pleasure to work with and around. The Nanolab community is strong and unique and I appreciate all the work you do. Similarly, I'd like to thank the graduate staff in the EECS department who helps us navigate complicated bureaucracy, and the staff in the Berkeley Sensor and Actuator Center.

Science does not occur in a vacuum, and I've been fortunate to work in two labs with extraordinary people whom I deeply admire. I cannot thank all of them by name, but I'd like to give a particular shout-out to Konlin Shen, who helped me find my bearings when I first joined; Oliver Chen and Jordan Edmunds, both of whom navigated the challenges of graduate school with me. The tail end of my PhD would not have been the same without Lydia Lee, whose intelligence, class, and humility constantly inspire me. Finally, Arda Ozilgen and Hani Gomez have both, in their own ways, helped usher in my successful completion of the doctorate and transition into professional life.

I want to thank the friends I came in with and those I have acquired at Berkeley, with whom I have danced, skied, backpacked, and, my favorite pastime of all, had deep and silly conversations. The constraints on this page do not allow me to list all of you. I hope to have you in my life for all the years to come. A particular mention to the roommates that have become family.

Which leads me to the end. I'd like to thank my family. A special mention to my cousin Martín, who is also my closest friend and who has participated in and gotten to know all of the many worlds I have inhabited–I cannot imagine a deeper bond than that one.

I'd like to thank my brother, Carlos Francisco, for modeling the virtues of hard work from an early age, and for giving me my nephews, Simón and Agustín. And to my sister, to whom this thesis is dedicated, I cannot express enough my thanks for your support and my admiration for your accomplishments. Finally, to my parents: ellos, que me enseñaron el valor del trabajo duro y la humildad, y que han dedicado su tiempo y su sudor a nuestra crianza. A mi papá, por ser un modelo de dedicación insuperable, y a mi mamá, por

enseñarme a navegar las relaciones humanas con la gracia que solo ella tiene. Les quiero mucho.

Chapter 1

Background and state of the art

1.1 Motivation

It is well known that life at the microscale is very different from what we usually experience. Science fiction is riddled with tales of miniature swimming devices that can help us explore the human body and multiple aqueous environments such as deep-sea vents. However, there is a wide gap between imagination and what has been achieved in this domain.

Microswimmers have a vast set of potential applications. Richard Feynman, in his famous talk "Plenty of room at the bottom"[13], suggests the possibility of "swallowing the surgeon", as proposed by Alfred Hibbs. In general, microswimmers could enable minimally invasive medicine, such as drug delivery, assisted fertilization, physiological detection, and improved biomedical imaging [5, 21]. Beyond medical applications, researchers have envisioned microswimmers exploring and collecting information in places unreachable by other means. For example, NASA SWIM (Sensing with Independent Microswimmers) aims to develop such devices for underwater exploration in extraterrestrial bodies of water and other liquids [37].

Most of the microswimmers developed, thus far, fundamentally rely on an external source of energy and control. For many applications, full autonomy is desirable so that the microswimmer can react to its local environment. This work focuses on propulsion mechanisms that can be locally controlled, even if they depend on external sources of energy. Local control of microswimmers enables for a whole array of new applications. For example, in a situation with multiple microswimmers in the same environment, local control allows each swimmer to act individually in a scalable manner. Autonomous devices should be able to react to their surroundings and sensor information, enabling phototactic and chemotactic behaviors without external closed-loop control. Additionally, in situations where our microswimmers go beyond the reach of the communication mechanism, it is useful to control propulsion at the device level.

Figure 1.1 shows an idealized microswimmer equipped with a microcontroller, a power source, and a propulsion mechanism. Ideally the devices in this dissertation can carry a
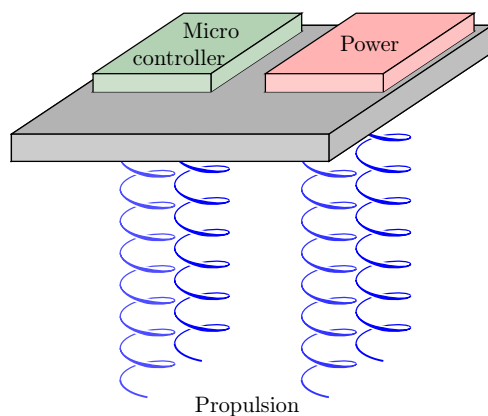
Figure 1.1: Anatomy of a microswimmer: the device consists of a propulsion mechanism, such as 4 flagella; a microcontroller brain, such as SCµM [28]; and a power source, such as [35].

CMOS brain, such as the Single Chip Micro-Mote (SCµM) [28] to make decisions. Thus, this work seeks to use a propulsion mechanism that can be easily controlled by electrical signals on the device itself. Ideally, these signals would be low enough voltage to be compatible with standard modern CMOS technologies. However, high-voltage drivers can be produced and are available, such as a solar cell array (Zappy) which can output up to 330 V [35].

Given that the mechanisms seen in nature and engineering at larger scales will not work for small devices, one can turn to nature for inspiration. Bacteria effectively use a hellical flagella with a nanoscale, reversible, rotary motor [43].

This chapter presents an overview of the relevant physical phenomena for our small-scale swimmers and discuss a few existing technologies in this space. The main concepts behind this dissertation are briefly introduced in order to properly contextualize the topics introduced during the rest of this chapter. The devices in this dissertation are electrostatically actuated, rotary inchworm motors. These are fabricated using an SOI process with the bonding of a lid to protect the devices from operation. Furthermore, water infiltrating the electrostatic motors must be avoided (see section 2.4 for more detail), so this work employs a hermetic packaging with a mechanical feedthrough.

1.2 Existing microswimmers

Research into microswimmer propulsion has been extensive – several mechanisms have been developed and demonstrated to swim and navigate aqueous environments. Here, these have been organized into categories and examples of each are provided. Note that some works will not fit neatly into these categories, but these can still be use as starting points for discussion on their advantages and limitations. A common thread among known microswimmer technologies is that any controllability comes from external fields, be it optical, magnetic, or acoustic. This often requires large, complicated equipment. While this is suitable for certain applications, such as biomedical procedures in a hospital, it limits field work. This work advances the state-of-the-art approach toward the use of electrostatic MEMS for underwater control.

For a recent review on biomedical swimmers, see [47]. This work is limited to devices that are smaller than a few millimiters on the side.

A common source of propulsion for microswimmers is the production of bubbles [26]. This usually relies on the device operating in a chemically-reactive environment, such as hydrogen peroxide, together with a material, such as platinum, that catalyzes the production of hydrogen and oxygen gas [16]. Lasers have also been used to photothermally activate bubbles or generate cavitation sites [30]. Additionally, there are recent developments to use electrolysis for bubble rockets, with an external optical power source [29]. This last option is distinct in that, despite using an external power source, the microswimmer could react be controlled by local, electrical signals.

Other microswimmers harness acoustic waves as sources of energy and propulsion. Acoustic streaming, the flow perpendicular to a vibrating surface in a nonlinear flow regime, is an attractive way to harness the power of acoustics. For example, oscillating pined bubbles generate a powerful streaming flow that can be used for propulsion [3]. Other promising advances use materials that change shape with light, together with structured light to deform and move them [31]. This is useful for small payloads and with optical access to the microswimmers.

Magnetic waves have also been used to manipulate devices with ferromagnetic materials [20, 5]. These include soft microrobots as well as flagellar or screw-shaped microrobots [48].

1.3 The fluid dynamics of microswimmers

To properly design a swimming microrobot, it is essential to understand the flow of fluid on a small scale. Assuming an incompressible fluid, the the Navier-Stokes equation governing fluid flow can be written as:

$$\rho \left(\frac{\partial}{\partial t} + \mathbf{u} \cdot \nabla \right) \mathbf{u} = -\nabla p + \mu \nabla^2 \mathbf{u} + \mathbf{g}, \tag{1.1}$$

$$\nabla \cdot \mathbf{u} = 0 \tag{1.2}$$

Here, $\mathbf{u}$ is the velocity field, ρ is the mass density, p is the pressure, μ is the dynamic viscosity, and $\mathbf{g}$ is a body force – such as gravity. Equations (1.1) and (1.2), represent the conservation of momentum (Newton's second law) and the conservation of mass for an incompressible fluid, respectively.

In order to better understand the scaling of forces to a microswimmer, the following non-dimensional parameters are introduced:

$$\tilde{\mathbf{u}} = \frac{\mathbf{u}}{u_0}, \ \tilde{t} = \frac{t}{(L/u_0)}, \ \tilde{p} = \frac{p}{\mu u_0/L}, \ \tilde{\mathbf{r}} = \frac{\mathbf{r}}{L};$$

where u_0 is a characteristic velocity, and L a characteristic length. The symbol $\mathbf{r}$ is used as the spatial coordinate, in connection with the spatial derivatives ∇. In this case, u_0 is selected to be the velocity of the microswimmer relative to the fluid and L to be a characteristic dimension in this microswimmer.

The assumption that $\mathbf{g} \approx 0$ is used, since gravity is not relevant on this scale and there is no external body force. Using the change of variables above it follows:

$$\underbrace{\frac{\rho u_0 L}{\mu}}_{\text{Re}} \left(\frac{\partial}{\partial \tilde{t}} + \tilde{\mathbf{u}} \cdot \tilde{\nabla} \right) \tilde{\mathbf{u}} = -\tilde{\nabla}\tilde{p} + \tilde{\nabla}^2\tilde{\mathbf{u}}, \tag{1.3}$$

$$\tilde{\nabla} \cdot \tilde{\mathbf{u}} = 0. \tag{1.4}$$

Note that all the terms in the equation are now nondimensional. The Reynolds number on the left quantifies the ratio of inertial forces to viscous forces, and is defined as

$$\text{Re} = \frac{\text{Inertial Forces}}{\text{Viscous Forces}} = \frac{\rho u_0 L}{\mu}. \tag{1.5}$$

The Reynolds number (Re) is a very useful parameter for understanding fluid flow at different scales. When Re is large, the left-hand side of equation (1.3) dominates and viscous losses can be ignored. However, if Re is small, viscosity is the dominant force. For example, a swimmer with characteristic dimension $L = 500\,\mu\text{m}$ in water with viscosity of $1 \times 10^{-3}\,\text{Pa} \cdot \text{s}$ and density $\rho = 997\,\text{kg/m}^3$ at $u_0 = 1\,\text{mm/s}$, has a Reynolds number of approximately 0.5. In general, small-scale swimmers have low Reynolds numbers because L is really small.

Let Re $\to 0$ in equation (1.3) and re-dimensionalize, the expression for Stokes flow of an incompressible Newtonian fluid is obtained.

$$0 = -\nabla p + \mu \nabla^2 \mathbf{u} \tag{1.6}$$

.

Equation (1.6) leads to an important insight. Due to the small L, microswimmers operate in the low Reynolds number regime. The mechanisms typically envisioned for swimming are often ineffective on these scales, as stated by Purcell in his Scallop Theorem [33]. The motion at such small Reynolds numbers is time-independent. This means that reversing

a particular configuration moves the swimmer back to its starting position. On a larger scale, it would work akin to swimming in molasses: the mechanisms seen in nature and engineering at larger scales will not work for small devices. This dissertation contributes toward a bioinspired artificial flagellar motor at the microscale.

1.4 Surface tension

(a) Droplet on a surface with contact angle θ.

(b) Differential surface element with perpendicular radius of curvature ρ_1 and ρ_2.

(c) illustration of surface tension in a narrow but long channel.
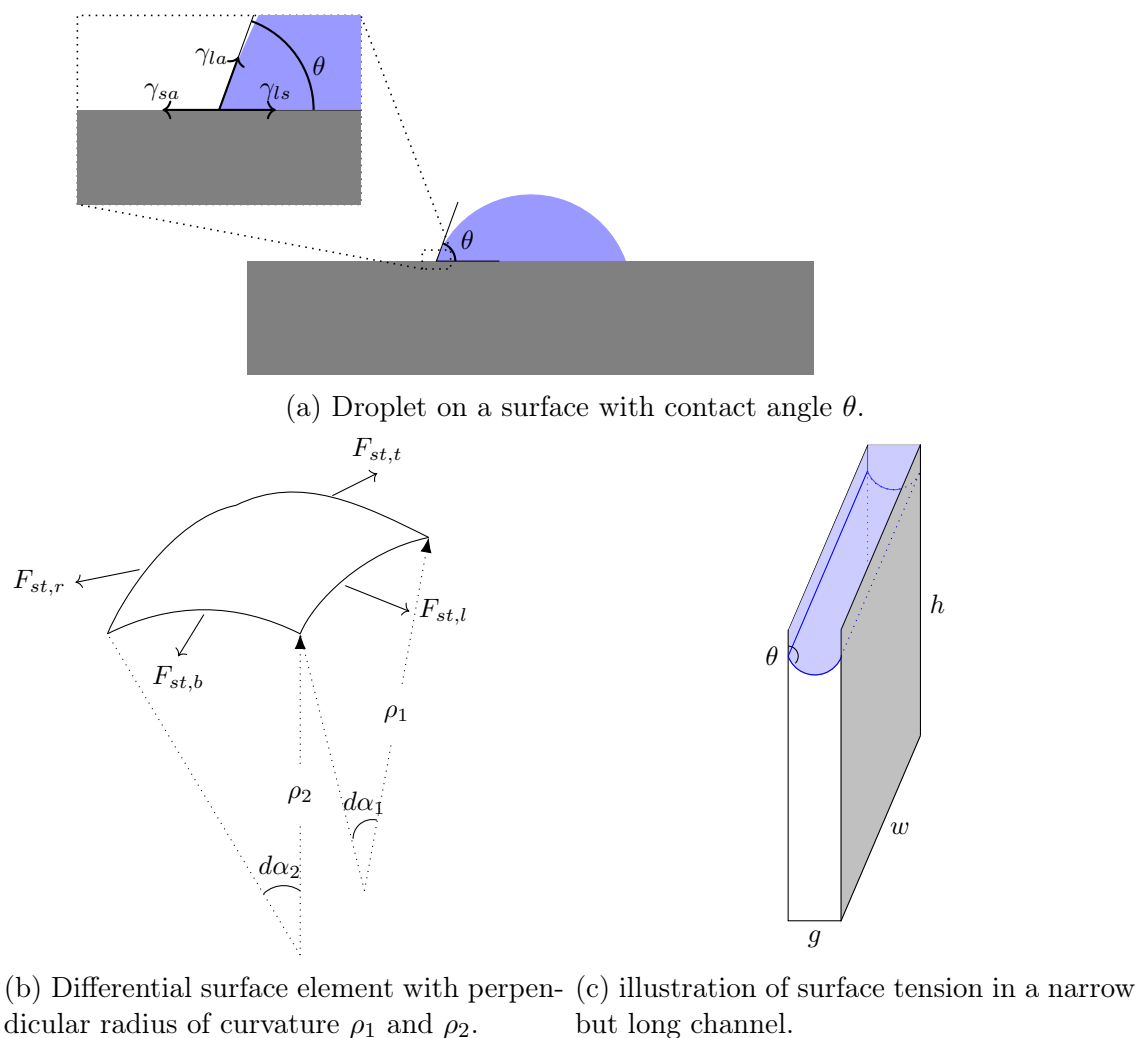
Figure 1.2: Surface tension and Laplace pressure.

When designing devices, surface tension and weight are often important. For an object of characteristic length ℓ, forces such as the weight scale with ℓ^3, while the surface tension is proportional to ℓ. Therefore, when things are scaled down to the microscale, surface tension

(also known as capillary forces) dominates. This is the phenomenom that allows insects to walk on water, a feat impossible for larger-scale animals [22].

This section provides a short introduction to surface tension and defines the terminology we will use to address it. For an overview of the challenges and opportunities surface tension presents in MEMS, see [22].

Fundamentally, surface tension is the tendency of liquid-gas interfaces to occupy the minimum possible surface area. This occurs because the liquid molecules exert a cohesive attraction on each other that is higher than the attraction of liquid molecules to the air.

As is often the case in physics, this phenomenon can be understood from a force or energy perspective. From a force perspective, we can think of liquid-air interfaces as a sheet of material under tension. The force tangent to the surface is

$$F_{st} = \gamma \ell,$$

where γ is the liquid-air surface tension of a material, with dimensions of force per unit length $\gamma = (72\,\mathrm{mN/m}$ for water-air surfaces at room temperature) and ℓ is length over which the force is considered. Some sources add a factor of $\frac{1}{2}$ because they consider F as the force from two surfaces.

We can also think of surface tension as an energy per surface area in $\mathrm{J/m^2}$. From a differential perspective, γ is the energy required to increase the surface by a certain amount. The surface energy of water is generally higher than that of other surfaces. This explains the tendency of water droplets to form spherical shapes, because spheres have the lowest surface-area-to-volume ratio.

1.4.1 Contact angle

The contact angle is a useful concept to capture the surface properties of a system. Just as the water-to-air (γ_{la}) has a surface energy, we can consider a value for the solid-air surface tension (γ_{sa}) and liquid-solid surface tension (γ_{ls}). Taking a force balance at the 3-state line, (see Figure (1.2a))

$$0 = -\gamma_{sa} + \gamma_{ls} + \gamma_{la} \cos \theta$$

$$\cos \theta = \frac{\gamma_{ls} - \gamma_{sa}}{\gamma_{la}}.$$

As showcased in the relation above, the contact angle θ captures the relationship between the three surface energies in a system with a liquid, a solid, and a gas.

When the liquid in consideration is water, surfaces with contact angles lower than 90° are considered hydrophilic, and surfaces with contact angles above 90° are considered hydrophobic. In other words, water on hydrophilic surfaces has a tendency to spread on the surface, whereas water on hydrophobic surfaces has a tendency to bead up.

The treatement above gives good intuitive understanding of surface tension, but it fails to consider additional factors. Non-idealized surfaces are not perfectly smooth. This, together with chemical properties, results in contact angle histeresis: there exists some friction

preventing the motion of the triple line on a surface. The concepts of advancing and receding contact angles capture the range of contact angles before the triple line advances or recedes on a moving droplet or bubble. For a more thorough explanation, see [22].

1.4.2 Laplace pressure

Any curvature in the surface results in a pressure differential across the surface. Consider a differential element as shown in Figure (1.2b). At rest, a force balance in the perpendicular direction results in

$$0 = \Delta p dA - \sin\left(\frac{d\alpha_2}{2}\right)(F_{st,l} + F_{st,r}) - \sin\left(\frac{d\alpha_1}{2}\right)(F_{st,b} + F_{st,t})$$

$$0 = \Delta p \rho_1 \rho_2 d\alpha_1 d\alpha_2 - \sin\left(\frac{d\alpha_2}{2}\right)(2\gamma\rho_1 d\alpha_1) - \sin\left(\frac{d\alpha_1}{2}\right)(2\gamma\rho_2 d\alpha_2) \quad \text{(since } d\alpha_1, d\alpha_2 \text{ are small)}$$

$$= \Delta p \rho_1 \rho_2 d\alpha_1 d\alpha_2 - \left(\frac{d\alpha_2}{2}\right)(2\gamma\rho_1 d\alpha_1) - \left(\frac{d\alpha_1}{2}\right)(2\gamma\rho_2 d\alpha_2)$$

Solving for Δp, we obtain the Young-Laplace equation:

$$\Delta p = \gamma\left(\frac{1}{\rho_1} + \frac{1}{\rho_2}\right).$$

Here γ is the value of surface tension, ρ_1, and ρ_2 are the radii of curvature in perpendicular relations, and Δp is the pressure differential between the inside and outside of the curved surface.

For these designs, $\rho_1 \gg \rho_2$ is often true, given one dimension is much smaller than the other, such as the situation depicted in Figure (1.2c). Assuming a contact angle of θ, and that g is small, the radius of curvature in this case is

$$\rho_1 = \frac{1}{2}\frac{g}{\cos\theta}.$$

Thus, the pressure differential due to surface tension is

$$\Delta p = \frac{2\gamma\cos\theta}{g}. \tag{1.7}$$

Equation (1.7), a form of the Young-Laplace equation, is fundamental to the designs in this disseration, as it outlines the pressure required for water to enter a gap g. We rely on this pressure differential being higher than the fluid pressure under which the devices operate, to prevent water ingress. Of particular importance to the fabrication process, hydrophobic surfaces ($\theta > 90°$) are needed to discourage the entry of water into sensitive structures that must remain dry for proper electrical operation. Section (2.1.1) dissects the importance of this.

1.4.3 Stiction

Of particular relevance to most MEMS devices is stiction, the tendency of structures to stick due to surface forces including surface tension. Consider two parallel plates that can move toward each other, with water in between. The force of surface tension pulling the plates together is given by

$$F = A\Delta p = \frac{2A\gamma\cos\theta}{g}$$

Again, note that if the surfaces are hydrophilic, $\cos\theta > 0$ and surface tension is a strong contributor to stiction.

In contrast, if the surfaces are hydrophobic, $\cos\theta < 0$ and surface tension does not contribute to stiction. In this case, surface tension has the opposite effect, preventing the surfaces from being brought together.

1.5 The dynamics of a flagellar motor
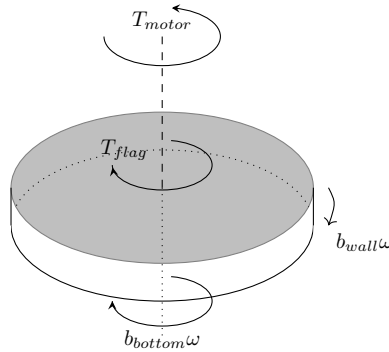
Figure 1.3: Torques acting on a central rotor shuttle.

Since this work focuses on building an artificial flagellar motor, we analyze the dynamics of swimming with a flagellum. Full details of the design and fabrication are given in Chapters (2 and 3). For the following analysis, we assume that the rotor and flagellum are submerged in water, for a conservative estimate of drag and speed.

Doing a torque balance on the central rotor, as depicted in Figure (1.3), we have

$$J_{rotor}\frac{d}{dt}\omega = T_{motor} - b\omega - T_{flag}, \tag{1.8}$$

where T_{motor} is the torque suplied by the motor, ω is the angular velocity of the rotor, and b is a drag coeffient computed below. J_{rotor} is the moment of inertia of the rotor, given by

$$J_{rotor} = \rho \frac{\pi t R^4}{2}$$

for a cylindrical disk of radius R and thickness t.

Given that we operate at small Reynolds numbers, we can set the acceleration $\frac{d}{dt}\omega = 0$, to compute the dynamics of a swimmer moving at constant velocity. Chapter (2) is dedicated to designing a motor that can supply T_{motor}.

1.5.1   Drag on the rotor

We separate drag on the rotor into two components:

$$b = b_{wall} + b_{bottom} \tag{1.9}$$

Here, b_{wall} is the drag viscous drag coefficient on the side walls of a cylindrical rotor and b_{bottom} is the drag of the cylinder over the substrate it sits on.

Low Reynolds number flow between two concentric cyclinders is called Taylor-Couette flow and is well studied. For a rotor of radius R and a gap to the sidewall g, the flow is described by [1]:

$$v_\theta = Ar + \frac{B}{r} \qquad \text{with}$$

$$A = \omega \frac{-\eta^2}{1 - \eta^2}, \qquad B = \omega R^2 \frac{1}{1 - \eta^2}, \qquad \eta = \frac{R}{R + g}.$$

With v_θ being the velocity profile as a function of radius, and μ the viscosity of the fluid. The shear at the wall is

$$\tau = \mu \left. \frac{\partial v_\theta}{\partial r} \right|_{r=R}$$

$$= \mu \left(A - \frac{B}{R^2} \right)$$

$$= \mu \left(-\omega \frac{R^2}{(R+g)^2 - R^2} - \omega \frac{(R+g)^2}{(R+g)^2 - R^2} \right)$$

$$= -\mu\omega \left(\frac{R^2 + (R+g)^2}{R^2 - (R+g)^2} \right)$$

Therefore, the total torque due to viscous drag on sidewalls of the shuttle is

$$T_{D,wall} = \tau Rt(2\pi R)$$

$$= \underbrace{-2\pi\mu R_1^2 h \left(\frac{R^2 + (R+g)^2}{R^2 - (R+g)^2} \right)}_{b_{wall}} \omega$$

$$= \underbrace{2\pi\mu R^2 t \left(\frac{2R^2 + 2Rg + g^2}{2Rg + g^2} \right)}_{b_{wall}} \omega$$

where t is the height of the cylinder.

Alternatively, a simpler expression for b_{wall} can be obtained assuming that R/g is large. If we assume parallel plate Couette flow and compute the torque over the whole circle:

$$T_{D,wall} = R\tau \times 2\pi Rt$$

$$= R \left(\mu \frac{R\omega}{g} \right) \times 2\pi Rt$$

$$= \underbrace{\frac{2\pi R^3 t\mu}{g}}_{b_{wall}} \omega.$$

The calculation of the drag on the bottom of the plate is similar. For simplicity, we assume a water film between the rotor and the substrate. We treat a differential element as though it has Couette flow with a linear profile, such that the shear stress for a film of height g_b is

$$\tau = \frac{\mu u}{t} = \frac{\mu r \omega}{g_b}$$

The torque for that individual element is

$$dT = \frac{\mu r \Omega}{g_b} r * r \ dr \ d\theta.$$

Integrating from $r = 0$ to $r = R$

$$T = \underbrace{\frac{\pi\mu R^4}{2g_b}}_{b_{bottom}} \omega,$$

and

$$b_{bottom} = \frac{\pi\mu R^4}{2g_b}.$$

Critically, the drag coefficient on the bottom plate is inversely proportional to g_b, the gap between the rotor and the plate. As fabricated, this gap is 2-3 µm in these devices, but the rotor shuttle can drop, resulting in smaller gaps.

During operation with a flagellum, the flagellum pulls the rotor away from the substrate.

1.5.2   Flagellar drag and thrust

Several models and theories of varying complexity exist to describe flagellar dynamics [36]. Although slender body theory and the Stokeslets method show better matching to experiments, here we use resistive force theory (RFT) with coefficients proposed by Gray and Hancock [15].
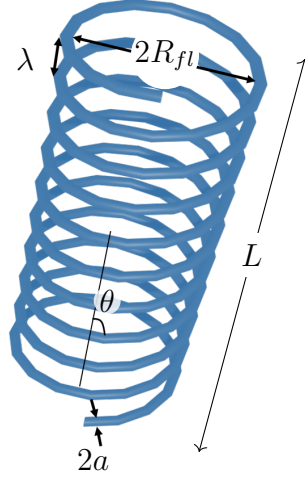
Figure 1.4: Important flagellar dimensions: period λ, revolving radius R_{fl}, angle from vertical θ, and filament radius a.

Consider a flagellum with dimensions outlined in Figure (1.4).

This results in overestimating thrust and drag and underestimating torque, depending on the $\frac{\lambda}{R}$ ratio. The expressions for thrust F_{flag}, torque T_{flag} and drag for a flagellum are given by

$$F_{flag} = (\omega R_{fl})(C_n - C_t)\sin\theta\cos\theta\frac{L}{\cos\theta}$$

$$T_{flag} = (\omega R_{fl}^2)(C_n\cos^2\theta + C_t\sin^2\theta)\frac{L}{\cos\theta}$$

$$D_{flag} = U(C_n\sin^2\theta + C_t\cos^2\theta)\frac{L}{\cos\theta}$$

D_{flag} will be used below, and is proportional t the velocity of the device U with respect to the fluid. With the drag coefficients of Gray and Hancock,

$$C_t = \frac{2\pi\mu}{\ln\frac{2\lambda}{a} - \frac{1}{2}}$$

$$C_n = \frac{4\pi\mu}{\ln\frac{2\lambda}{a} + \frac{1}{2}}$$

The coefficients above represent the tangent and normal contributions of the flagellum to thrust and provide insight into the inherent mechanism for flagellar propulsion.

From this, we note that

$$\frac{F_{flag}}{T_{flag}/R_{fl}} = f(a, \lambda, \theta) = f(a/R_{fl}, \lambda/R_{fl}).$$

In particular, the flagella converts the torque to thrust with the same efficiency regardless of length L. However, rotation rates and ultimate speed depend on L. This means that extending the length of the flagellum enables us to reach the same swimming velocities if we cannot increase motor speed but can increase torque.

If we non-dimesionalize the terms above, we have the following parameters

$$F^* = (C_n^* - C_t^*) \sin\theta \cos\theta \frac{(L/R_{fl})}{\cos\theta}$$

$$T^* = (C_n^* \cos^2\theta + C_t^* \sin^2\theta)\frac{L/R_{fl}}{\cos\theta}$$

$$D^* = (C_n^* \sin^2\theta + C_t^* \cos^2\theta)\frac{L/R_{fl}}{\cos\theta}$$

with the coefficients non-dimensionalized by μ. Now that we have a model for flagellar dynamics, we can have a basic model of motor operations.

1.5.3 Steady state motor operation

In this section, the steady state motor operation is analyzed to understand the necessary torque and speed considerations for the motors. Setting $\frac{d}{dt}\omega = 0$ in Equation (1.8)

$$T_{motor} = b\omega + T_{flag} \tag{1.10}$$

$$= (b_{wall} + b_{bottom} + T^* \mu R_{fl}^3)\,\omega \tag{1.11}$$

with b_{wall}, b_{bottom} and T^* are fully defined in the preceding sections based on the geometry.

1.6 Weight and neutral buoyancy

The weight of the device can be easily estimated from its volume and density

$$F_w = \rho_{dev} V g.$$

A 1-mm^3 piece of silicon ($\rho_{Si} \approx 2300\,\text{kg/m}^3$) has a weight of $22.6\,\mu\text{N}$, 3 orders of magnitude above the expected forces we can produce with a flagellar motor.
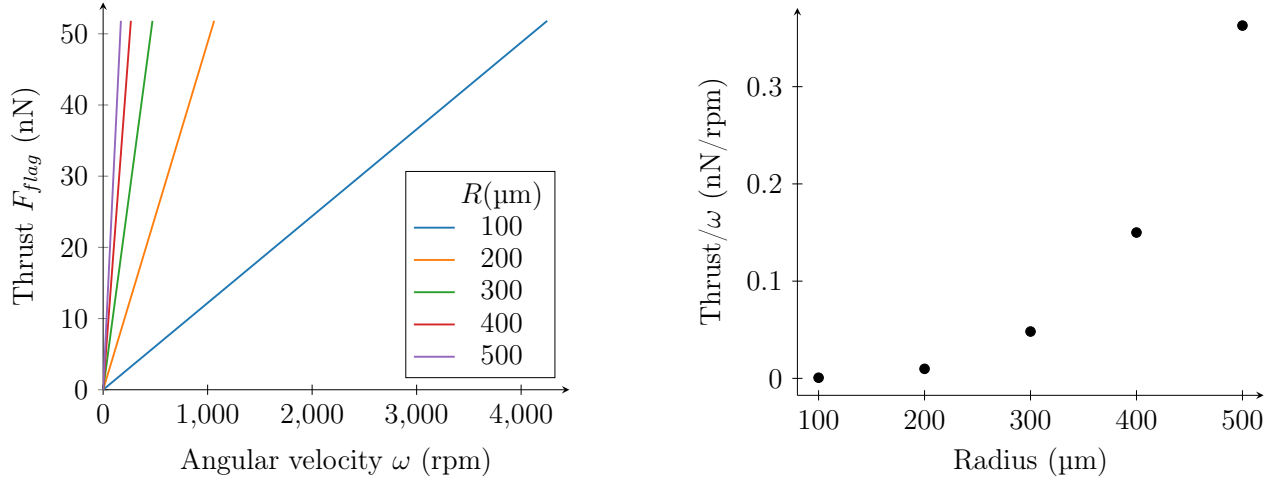
Figure 1.5: Flagellar dynamics assuming flagellar and shuttle radius are the same, $\lambda/R = 6.5$, $a/R = 1/7$. Left shows thrust produced by a flagellum with $L/R = 20$. The plot on the right is independent of L.

However, bouyancy acts on underwater devices equal to the weight of the water displayed and acts in the opposite direction

$$F_B = \rho_{H20} V g.$$

To achieve neutral buoyancy, we introduce air bubbles into the device, such that

$$\rho_{dev} = P_{Si}\rho_{Si} = \rho_{H20}$$

where P_{Si} is the proportion of the device. Thus, if a device has 43% silicon and the remaining is air, it becomes neutrally buoyant. In a preliminary study, we fabricated devices with a backside DRIE tuned to achieve the removal of 57% of the silicon.

Figure 1.6 shows an etch silicon microchip suspended in water. The chip was produced by DRIE etching $450\,\mu m$ into the silicon with a honey-comb pattern, out of a $670\,\mu m$ wafer thickness. A PECVD flouropolymer (3.2) was applied to hydrophobize the surface. The bubbles are trapped simply bu submerging the chip in water.

For the rest of the analysis, it is assumed that weight is not a significant force to overcome.

1.7 Microswimmer speed and motor requirements

A simple force balance of this motor at constant velocity, assuming neutral bouyancy, is

$$0 = ma = F_{flag} - F_{d,flag} - F_{d,substrate},$$
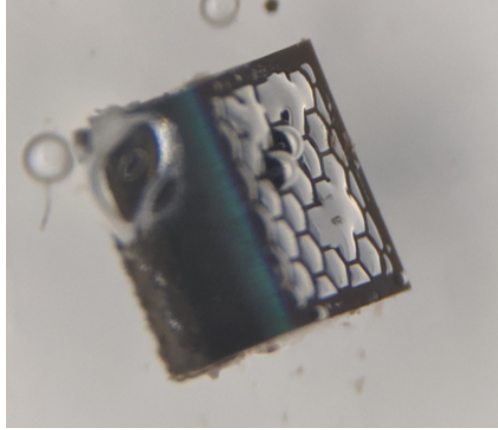
Figure 1.6: Neutral buoyancy achieved by hollow backside etch. The device is 1 mm × 1 mm × 670 μm and is suspended in water.

with F_{flag} the thrust force provided by the flagellum, $F_{d,flag}$ the drag on the flagellum and $F_{d,substrate}$ the drag on the substrate.

At low Reynolds number, the stokes drag on the substrate is given by [24]

$$F_{d,substrate} = \underbrace{3\pi\mu\left(\frac{d_n}{3} + 2\frac{d_s}{3}\right)}_{D_{subs}}U,$$

where $d_n = \frac{2\sqrt{A_n}}{\pi}$ for A_n the projected area normal to the direction of motion, and $d_s = \frac{\sqrt{A_s}}{\pi}$ for the surface area of the device A_s; essentially, these are the equivalent normal and surface area diameters.
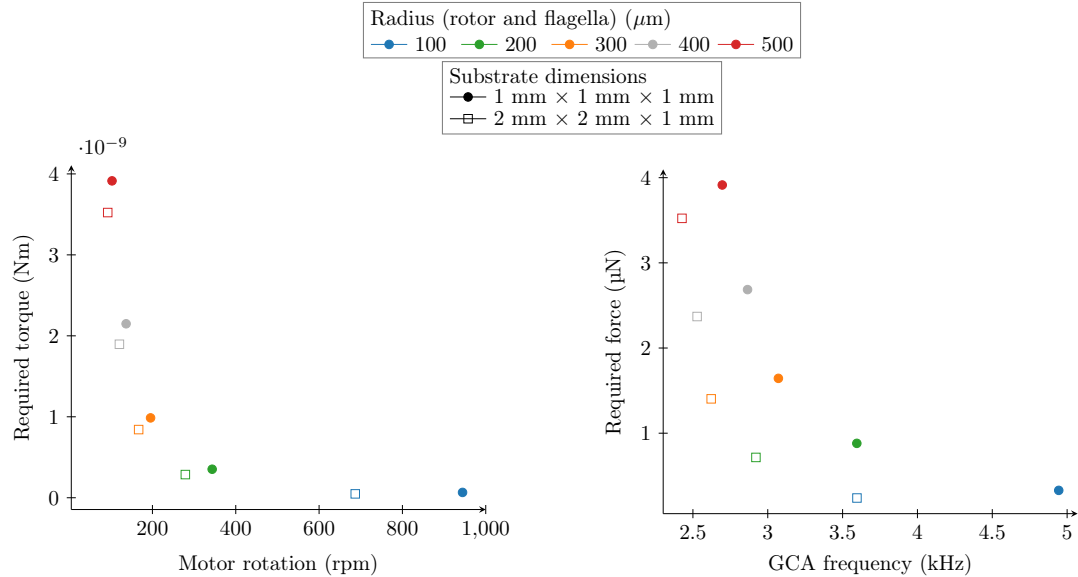
(a) Required torque and rotation for a flagellar microswimmer at 1 mm/s.

(b) Required force $\frac{T_{flag}}{2R}$ and Inchworm frequency for a flagellar microswimmer at 1 mm/s.

Figure 1.7: Estimated motor capability for a flagellar microswimmer at 1 mm/s. Plot (b) assumes every step of the GCA is 2 µm.

We make some reasonable assumptions of the size and geometry of the device, namely that the devices are 1 mm thick and have an area of $1\,\text{mm}^2$ and $2\,\text{mm}^2$.

Figure (1.7) shows estimates for required torque and motor velocity and their consequences for the rotational inchworm motors in this work. As a point of reference, we compute the efficiency of the swimming mechanism

$$\eta_{flag,subs} = \frac{P_{out}}{P_{in}} = \frac{F_{flag}v}{T_{flag}\omega}.$$

his is a metric of how well a flagellar mechanism with the parameters above converts the energy provided by the motor with a $1\,\text{mm}^3$ substrate. For the parameters above, η ranges from 0.08% to 0.12%. This efficiency accounts for energy lost due to viscous losses on the rotor, the flagellum, and the substrate. For comparison, *E. coli* flagella have a swimming efficiency of around 2% [4]. The lower efficiency presented here is due to the substrate being much larger in proportion to the flagellum compared to bacteria. The designs presented here account for realistic sizes given our current process capabilities and do not represent the optimal efficiency, as they do not reduce drag on the substrate

Now that the general charateristics of microswimmers have been established, the following chapters cover the design of rotational electrostatic inchworm motors (Chapter 2), their fabrication process (Chapter 3) and the electromecanical results of this work (Chapter 4).

Chapter 2

Device Design and Operation

2.1 Rotational Inchworm Motors

The devices in this dissertation are all variations of rotational, angled arm, inchworm motors. The design is inspired by the linear inchworm motors developed by Penskiy [32], with modifications to enable roation and underwater operation. Figure (2.1) shows the device concept. The device consists of four gap-closing actuators (GCAs), each with a flexible angled arm. Oposite pairs are actuated together, exerting torque on the rotational shuttle. Every cycle, the central shuttle rotates a small step with larger force exerted by high force density GCAs.

Each gap-closing actuator consists of an array of interdigitated fingers with a smaller gap g_1 in front and a larger gap g_1 in the back. The movable electrodes are mechanically connected to springs that are compliant in the y direction, but stiff in x. Figure (2.3) shows the main design features and important dimensions of a GCA. The capacitance of a gap-closing actuator, as a function of the distance y the movable electrodes have translated is given by

$$C_{GCA}(y) = \epsilon_0 \epsilon_r N t L_{ol} \left(\frac{1}{g_1 - y} + \frac{1}{g_2 + y} \right) \tag{2.1}$$

Here, L_{ol} is the overlap between to fingers, ϵ_0 is the permitivity of free space, N is the number of fingers, and t is the device thickness.

The electrostatic energy stored in this capacitor is

$$E_{es} = \frac{1}{2} C_{GCA}(y) V^2.$$

The voltage V is applied across the GCA fingers by grounding movable fingers throught
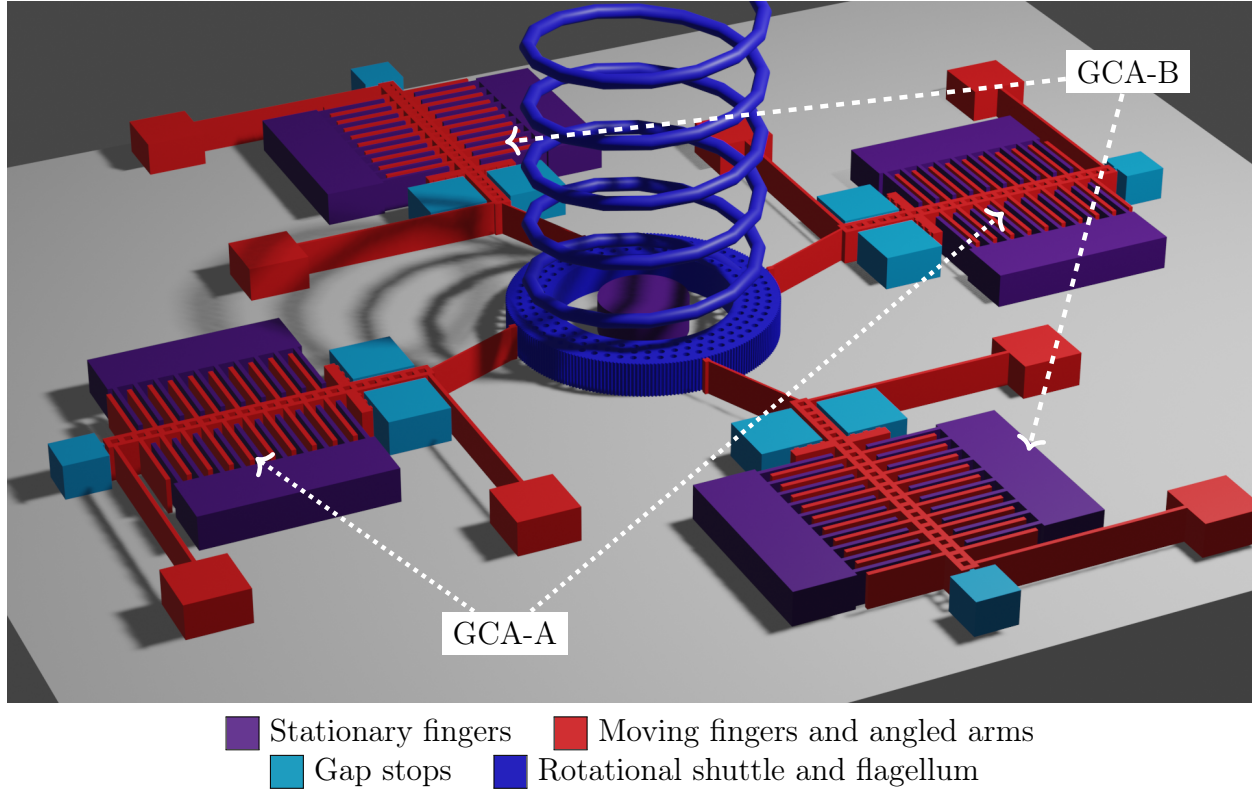
Figure 2.1: Device overview: Rotational inchworm motor. The motor consists of four gap closing actuators with flexible angled arms, that turn a central shuttle with a flagellum attached.

the support springs and therefore, when a voltage is applied, a the force is given by:

$$F_{es}(y) = \frac{d}{dy} E_{es} \tag{2.2}$$

$$= \epsilon_0 \epsilon_r N t L_{ol} \left(\frac{1}{(g_1 - y)^2} - \frac{1}{(g_2 + y)^2} \right) V^2. \tag{2.3}$$

This force gets translated into rotation of the central shuttle by an angled arm with a toothed pawl at the end.

The device operates as follows (see Figure (2.2) for timing):

1. First the GCA-A and GCA-B are engaged.

2. The voltage for GCA-A is turned off.

3. The voltage for GCA-A is turned back on. As the pawls engage they push the shuttle to rotate by one step.
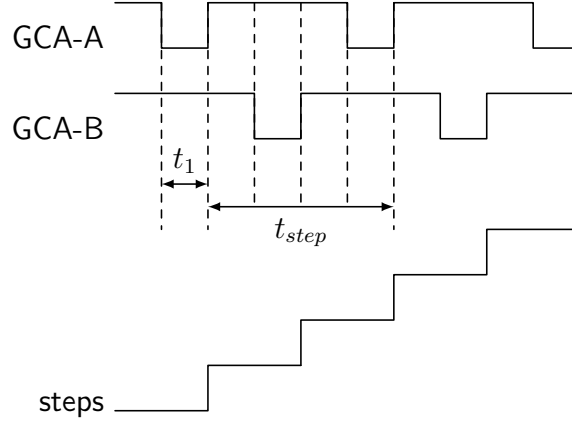
Figure 2.2: Rotational inchworm actuation sequence.

4. The voltage for GCA-B is turned off.

5. The voltage for GCA-B is turned back on. As GCA-B engages the shuttle rotates by another step.

6. Steps 2-5 are repeated over the whole range of operation.

For gap-closing actuators, if the voltage is high enough to close $1/3$ of the gap, the device becomes unstable and "pulls in". To prevent shorting and welding of devices togehter, a gap stop is introduced. The maximum capacitance (and maximum force) of a GCA occurs for $y = g_1 - g_s$, where g_s is the minimum gap

$$
\begin{aligned}
C_{GCA,\text{max}} &= C_{GCA}(y = g_1 - g_s) \\
&= \epsilon_0 \epsilon_r N t L_{ol} \left(\frac{1}{g_s} + \frac{1}{g_2 + g_1 - g_s} \right)
\end{aligned}
$$

This operation dynamic described above is the same as that used by [32] for linear electrostatic inchworm motors. The main difference with this work is the positioning of the pawl actuators and the shape of the central shuttle. Not all of F_{es} gets transfered onto the angled arm:

$$
F_y = F_{es} - k_s \Delta y \tag{2.4}
$$

Here k_s is the spring constant of the parallel beams attached to the shuttle, which can be computed from standard beam theory for a clamped-guided beam:

$$
k_s = \frac{E t w_s^3}{L_s^3} \tag{2.5}
$$
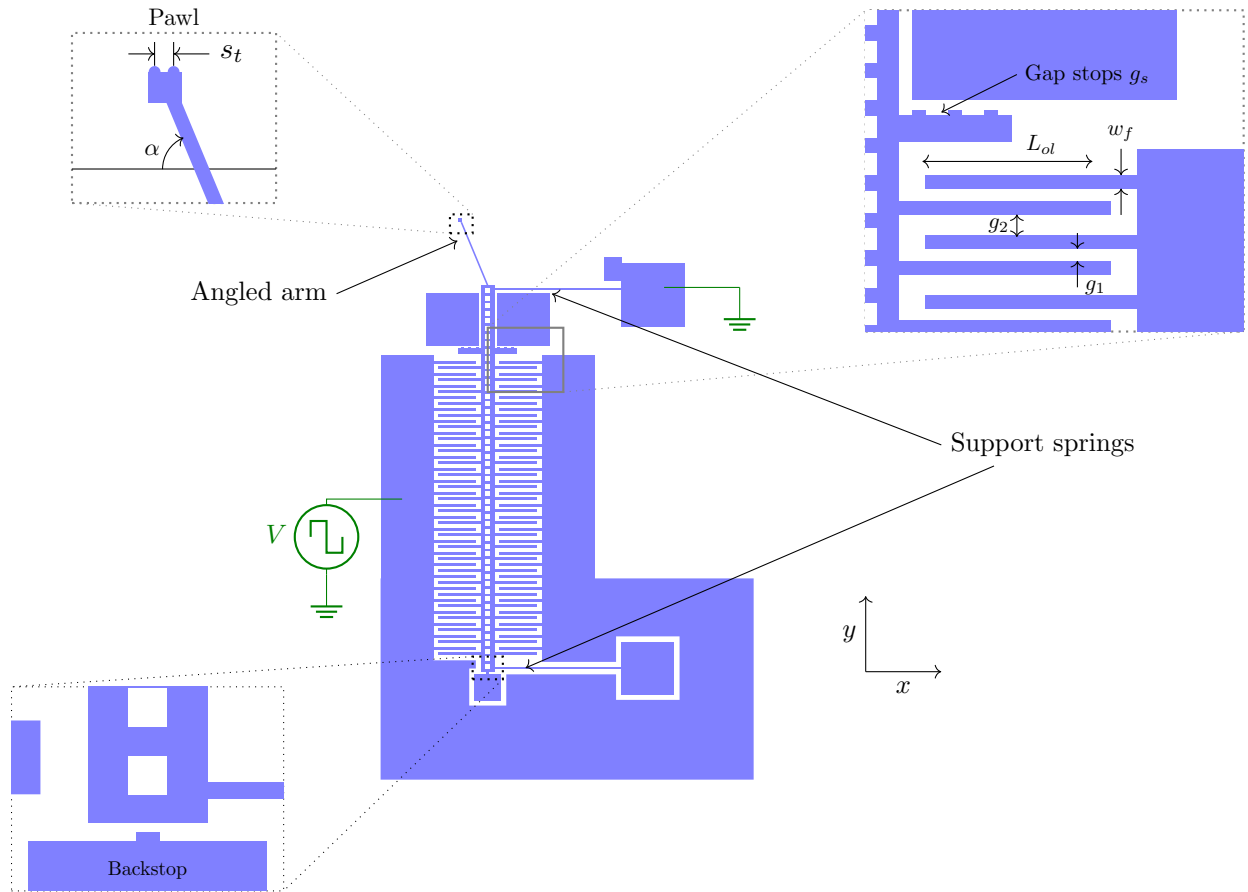
Figure 2.3: Layout of single gap closing actuator (GCA). Insets show important dimensions, the pawl that makes contact with the roational shuttle and the backstop to make sure $g_1 < g_2$ is preserved. Electrical connections are shown in green.

where E is Young's modulus, t is the device thickness, w_s is the spring width, and L_s is the lenght of the spring.

Although smaller spring constants are desirable to increase the force delivered to the shuttle, the springs need to be robust enough to provide a restoring force when the GCAs are disengaged.

Moreover, the device must operate significantly below resonance, in a quasi-static regime. Mechanical systems at resonance have the maximum kinetic energy equal to the maximum potential energy in the spring. This means that the force delivered to the shuttle would be minimized, which is undesirable. Similarly to [32], the GCAs are designed to have a resonance frequency of at least $10\,\mathrm{kHz}$ to guarantee sufficiently robust springs and ensure it will not approach resonance during operation.

Assuming the central shuttle radius is large enough, the force tangent to the shuttle

exerted by the angle arm is given by [32]:

$$F_x = \frac{F_y}{\tan \alpha} - K_\phi \frac{\Delta x}{L_{arm}^2 \sin^2 \alpha}$$

Here, F_x is the force exerted tangent to the shuttle, α is the angle of the angled transfer arm, and Δx is the step size tangent to the shuttle. The first term above represents the x component when the angled arm transfers the GCA force, while the second component is the force absorbed by the flexure of the angle arm. The rotational spring constant of the angled arm can be estimated as

$$K_\phi = \frac{I_{arm}E}{L_{arm}} = \frac{1}{12} \frac{t b_{arm}^3}{L_{arm}}.$$

In order to maximize the output force, the angled arm is designed to be as flexible as possible while preventing buckling.

For the output force of this device, consider the minimum force it delivers

$$F_{x,out} = \frac{F_y}{\tan \alpha} = \frac{F_{es}(\Delta y_{eng}) - k_s \Delta y_{eng}}{\tan \alpha}$$

where Δy_{eng} is the amount the gaps must close before the shuttle engages. In this equation, the losses due to K_ϕ are not included, because the minimum force is delivered to the shuttle upon engagement. As the gaps close further, the electrostatic force increases much faster than the losses due to the angled arm flexing, especially since the length of the arm is chosen to minimize losses.

The details that are important for the computations below are discussed in this section. For a complete and detailed methodology, please see [32]. For this work, a Python tool that integrates Penskiy's optimization and passes the results to a layout library was developed. This essentially constitutes a rotational inchworm motor automatic generator, that could be used in future reaserch to quickly layout devices with different force and electrical characteristics than what has been chosen below.

2.1.1 Power consumption

The average power consumption of gap-closing actuators can be estimated based on the energy required to charge a capactitor

$$
\begin{aligned}
E &= \int_0^V QV \ dV \\
&= \int_0^V C_{GCA}(V)V \ dV \\
&\leq \int_0^V C_{GCA,\text{max}}V \ dV \\
&= \frac{1}{2}C_{GCA,\text{max}}V^2.
\end{aligned}
$$

For a frequency of charging and discharging f, the average power is

$$P = \frac{1}{2}C_{GCA,\text{max}}V^2 f. \tag{2.6}$$

This equation is a simplification based on a number of assumptions. First, it is assumed that the capacitor is driven with a square wave, with $C_{GCA}V^2$ of energy provided by the power supply. Under these conditions, half of the energy is lost independent of the resistance. Better charging effiency can be obtained with pseudo-adiabatic charging circuits, where the voltage is increased in several steps [25].

Operation of GCAs underwater

Electrostatic gap-closing actuators have previously been demonstrated to operate underwater [40]. Given the relative dielectric constant of $\epsilon_r \approx 80$ for water, operating underwater requires lower voltages, with voltages around 6 V (compared to 50V for air for being enough for proper operation. However, even dionized water is somewhat conductive, and farradaic currents leading to electrolysis flow above a few volts (3.1 V in these experiments). Not only would bubbles prevent smooth mechanical operation, but faradaic currents would short the capacitor. To bypass this, Shih operated the GCAs with square waves at MHz frequencies, high enough to avoid charge screening. The required frequency is a function of the electrical conductivity and, hence, ion concentration of the aqueous environment of operation [42].
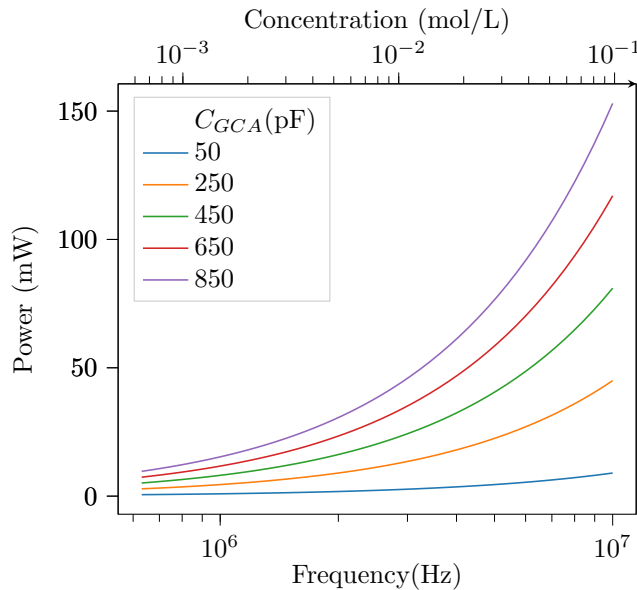

Figure 2.4: Power consumption for GCAs operating underwater over a range of device capacitances. The computation assumes a 2 nm native oxide. The necessary frequency of operation is mapped to the ion concentration in the environment based on [42].

Figure 2.4 shows the power consumption for a range of capacitances that would be required and result from wet GCA operation across ion concentrations common in natural settings. Here, we assume the validity of equation 2.6. For MHz operation, pseudo adiabatic circuits are not feasible [25]. Driving the circuit with an inductor, thereby creating an electrical oscilator is another possiblity, limited by the Q factor of the inductor and the intrinsic resistance in our devices.

Devices that operate in a fully inmersed mode have power requirements outside of the realm of possibility for microrobots. For reference, solar cells can output $110\,\mu\text{W/mm}^2$ at 1 sun [35]; a piezoelectric oscillator can can harvest $330\,\mu\text{W/mm}^3$ from ultrasound at 1/10 of the FDA limit for human operation[41]; and microbatteries have been demonstrated with an areal power desnity of $26\,\mu\text{W/mm}^2$. Although higher power density sources and more efficient capacitor charging methods might be strictly physically possible, practical sources of energy are orders of magnitude away from supplying the necessary power for wet GCA operation.

Hermetic packaging with a mechanical feedthrough for GCA operation

Because fully submerged operation is not viable, a design that keeps the gap-closing actuators dry was used, allowing operation at relatively low frequencies.

The description hermetic operation with a mechanical feedthrough refers to devices where the gap-closing actuators are dry and surrounded by water, but the rotor and flagellum can make contact with water.

2.2 Torque and Speed

Using equations above, the torque delivered by a single GCA onto the central shuttle would be

$$\begin{aligned} T_{GCA} &= R_{shuttle} F_{x,out} \\ &= R_{shuttle} \left(\frac{F_{es}(\Delta y_{eng}) - k_s \Delta y_{eng}}{\tan \alpha} \right) \end{aligned}$$

Since a GCA pair, the torque delivered to the rotor is

$$T_{GCA,A} = 2 * R_{shuttle} F_{x,out}$$

$T_{GCA,A}$ is the appropriate quantity to compare with the requirements determined in Chapter 1. It is important to note this is not the stall torque of the motor, but rather the torque with which it can prefrom steps of size Δ .

The rotational speed of the shuttle depends on two main constraints. First, that the motor can sustain enough torque to overcome drag on the shuttle and flagellum. The other

constraint is that the motor can operate at a frequency high enough to reach desired speeds. This second constrain is mainly limited by the pull-in and pull-out time of the gap-closing actuators, which is discussed in the following section.

2.2.1 GCA motor dynamics

A key factor on the speed of electrostatic inchworm motors is the pull-in and pull-out times. The dynamics are modeled with a standard mass-spring-damper differential equation, with the model proposed and validated by Contreras [8]

$$F_{es}(y) = m_{GCA}\ddot{y} + b_{GCA}\dot{y} + k_{sp}y.$$

The above parameters are the mass of the GCA, a damping coefficient b_{GCA} and the spring constant of equation (2.5). The exteral force applied is the electrostatic force defined in equation (2.1).

A differential equation solver was used to compute pull-in and pull-out for each of these designs. In the case of pull-in, it is defined as the time it takes for the gap stop to touch. For pull-out, however, two different times are computed

- $t_{pull-out}$: the time for the GCA to first reach its neutral position

- $t_{pull-out,1\mu m}$: the time for the ringing to be lower than $1\,\mu m$ of amplitude.

The second item listed here is needed because, in this work, unlike [8], the shuttle only hits the backstop at $y = -3\,\mu m$. This is due to the lithography definition of $2\,\mu m$ plus an additional $1\,\mu m$ from the DRIE undercut.

As a useful figure of merit for motor speed, the maximum frequency of operation is computed as

$$f_{\max} = \frac{1}{t_{pull-in} + t_{pull-out,1\mu m}}$$

2.2.2 Typical device design

The design follows the constraint above, with a GCA geometry that maximized force per unit area, with the rationale and methodology outlined by Penskiy [32]. This work was done by optimizing for the maximum force per unit area, since although the necessary forces are relatively low, the devices will include surface forces and friction that could dominate the necessary force output. The fabrication limitations are the same, a minimum feature size of $2\,\mu m$ determined by lithography and an aspect ratio of 20:1 determined by DRIE limitations.

Table 2.1 shows the design parameters that are kept constant throughout the designs. These are chosen to optimize the force delivered to the central rotor. $\Delta x = 2\,\mu m$ was picked based on the minimum feature, and spaced the teeth such that after GCA-A and GCA-B go through a full cycle, the shuttle has moved by $4\,\mu m$ on its outer radius. For critical size
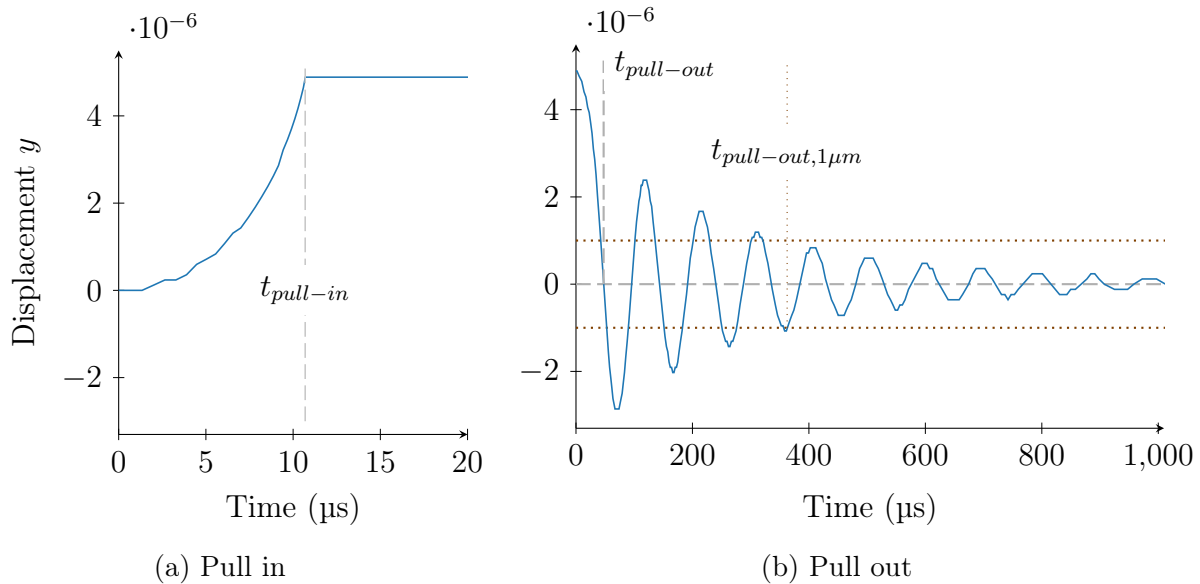
(a) Pull in

(b) Pull out

Figure 2.5: Example pull-in and pull-out time computations. Data shown in plot corresponds to device 2A.

parameters, such as gaps and widths, the parameters reflect the expected size as fabricated. During the layout process, the lines were widened by $1\,\mu m$ and the spaces were reduced by the same amount, to account for a $500\,nm$ undercut during the DRIE process [8]. Etch hole size was determined by process constraints.

2.3 First-generation devices and test structures

The goal of the first generation of devices was to develop the fabrication process and provide data to improve for the second generation devices. To that end, several test structures were designed and a few candidate devices. This section outlines the devices fabricated in the first round and their purpose.

2.3.1 Rotary inchworm motors

Three variations of rotary inchworm motors were included in the first mask, with characteristics shown in Table 2.2. All devices have the same GCA design, as there was experience with linear motors indicating that this design would work well.

Figure 2.6 shows an example of a generation 1 device. The device The main variations in the device are based on the rotor radius and hub type.

The central rotor has a via defined over it. This provides visual access to the central rotor and eventually acts as a mechanical feed-through for the flagellum. The via is smaller

Table 2.1: Design parameters used across all motors

Parameter	Description	Value
t	Device layer thickness	$40\,\mu m$
g_1	Small capacitor gap	$5.85\,\mu m$
g_2	Large capacitor gap	$8.77\,\mu m$
g_s	Gap stop size	$1\,\mu m$
w_f	Finger width	$4\,\mu m$
α	Flexible arm angle	$67°$
w_{arm}	Angled arm width	$2\,\mu m$
$V_{\max}$	Maximum voltage	$120\,V$
w_{etch}	Etch hole width or diameter	$8\,\mu m$
w_s	Spring width	$2\,\mu m$
w_s	Spring width	$2\,\mu m$
Δx	Step size at pawl	$2\,\mu m$
s_t	Pawl tooth pitch	$4\,\mu m$

than the rotor radius itself, to prevent us from loosing the rotor once it has been released.

For the first generation, there are two hub types: the central shuttle occupies the entire area (labeled None in Table 2.2), or a single rotational spring attached to a hub in the center. This spring serves two purposes: first, it keeps the rotary shuttle attached after release for test runs with only a single wafer; and second, as a known spring constant to estimate the force produced by these motors. Using a single spring as a tether to be broken before testing worked well to obtain preliminary results. However, with the spring present the devices did not operate well. This is an important lesson for rotary designs. Symmetry is paramount.

For proper testing when covered, the signals out to probing pads were routed with vias defined on the top wafer (top via in the diagrams). In practice, it was found that these vias were too small for the tungsten probes to land on the pad without touching the substrate of the top wafer. This is because probes approach pads at an angle in the probe station setup. For testing of first-generation devices this was circumvented by uncovering a much larger bond pad region using smaller lids and die-level bonding.

Other notable features of this design include the use of serpentine springs to connect all movable fingers arrays to ground. Since the pawls might come in contact with aqueous solutions, it is important the the movable fingers are grounded to prevent shorting between GCA-A and GCA-B.

2.3.2 Structures for 2-layer routing

One of the limitations of a simple, single-SOI-wafer process like that used by previous works [39, 32, 8], is that all routing must be done in a single layer. This results in the need for
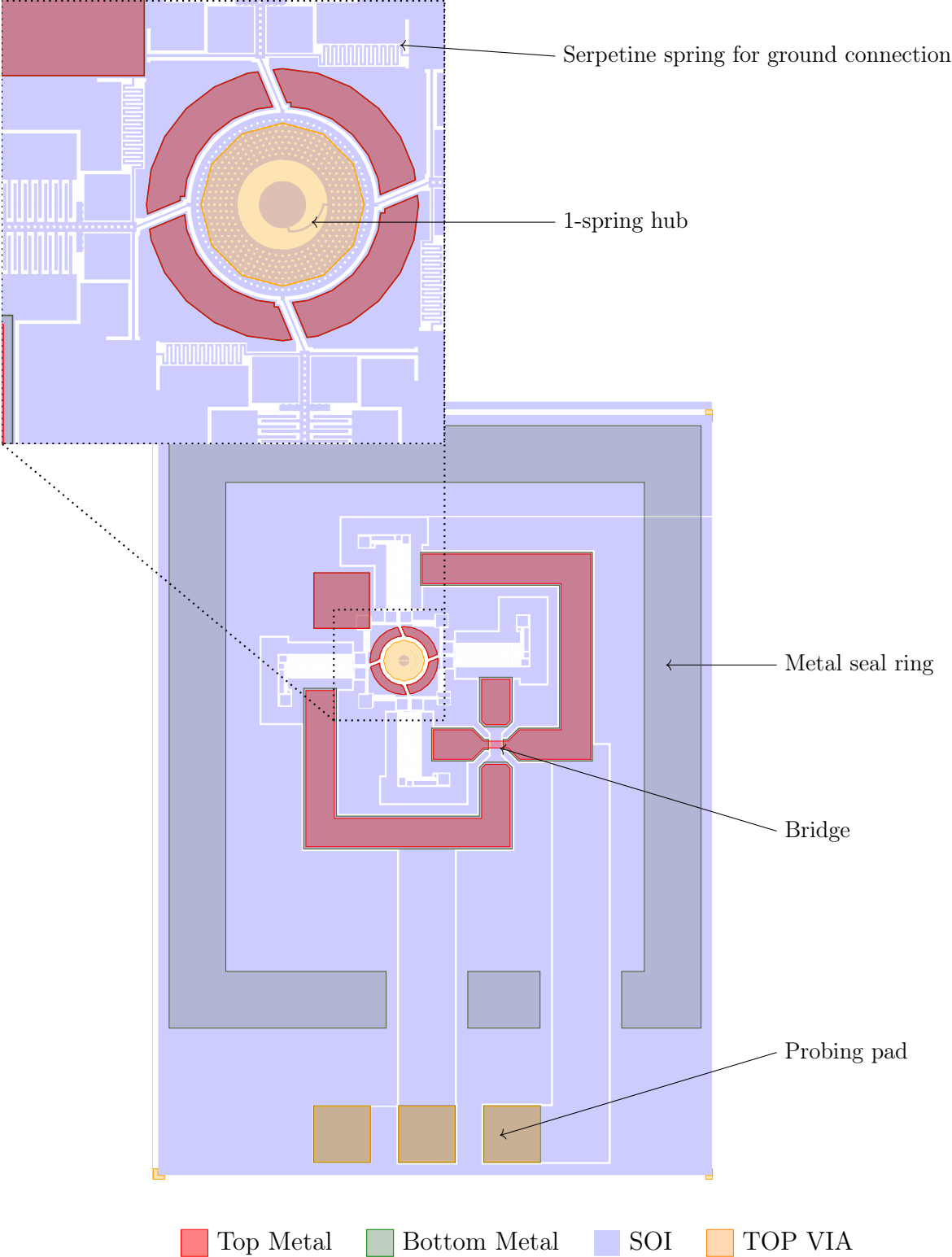
Serpetine spring for ground connection

1-spring hub

Metal seal ring

Bridge

Probing pad

Top Metal Bottom Metal SOI TOP VIA

Figure 2.6: Typical first generation device (Motor 1B).

Table 2.2: Characteristics of first-generation rotary motors

Parameter	Symbol	1A	1B	1C	Unit
External shuttle radius	$R_{shuttle}$	200		500	µm
Internal shuttle radius	R_{in}	0	100		µm
Hub type	-	None	1-spring		-
Number of fingers per GCA	N	50			-
Overlap finger length	L_{ol}	75			µm
Spring lengths	L_s	240.8			µm
Initial capacitance GCA-A	$C_{GCA}(y=0)$	0.76			pF
Maximum capacitance GCA-A	$C_{GCA,\mathrm{max}}$	2.73			pF
Spring constant	k_{spr}	15.1			kHz
Angled arm length	L_{arm}	125			µm
GCA resonance frequency	f_{res}	12.2			kHz
Pull-in time	$t_{pull-in}$	10			µs
Pull-out time	$t_{pull-out,1\mu m}$	273.9			µs
Maximum operation frequency	f_{max}	3.52			kHz
GCA efficiency	η	23.7%			-
Output force at 120 V	$F_{x,out}$	1.13			mN
Output torque at 120 V	$T_{GCA,A}$	453		1131	nN m
Power consumption at 120 V, 1 kHz	P_{total}	19.64			µJ

several external connections, which would be inconvenient for practical microrobots. To that end, the need for a bonded wafer was leveraged to introduce a second layer of routing. Figure (2.7) shows how one signal over another was done using a "bridge". Functionality can be checked by measuring the resistance of both traces independently and confirming that there are no shorts between both. In addition to confirming that it was possible to jump over signals, measuring the contact resistance of the bonds as a proxy for bond quality was necessary. Figure (2.8) shows a structure designed to perform 4-point measurements and calculate contact resistance as a function of area. The area of contact between the top trace and the bottom trace remains constant unless there is significant misalignment in θ, which is unexpected.

2.3.3 Additional test structures

Beyond the structures described above, test structures for process tuning and lithography were included, as well as independent motor components such as GCAs (with array variations over finger length and spring constant). These were included as basic safeguards to feed into second-generation designs.

Top trace

Bottom trace

Top trace

Bottom trace

Top Metal
Bottom Metal
SOI

Single Crystal Silicon
ALD Alumina (Al_2O_3)
Buried SiO_2
Ti-Pt-Au

(a) Layout

(b) Cross section
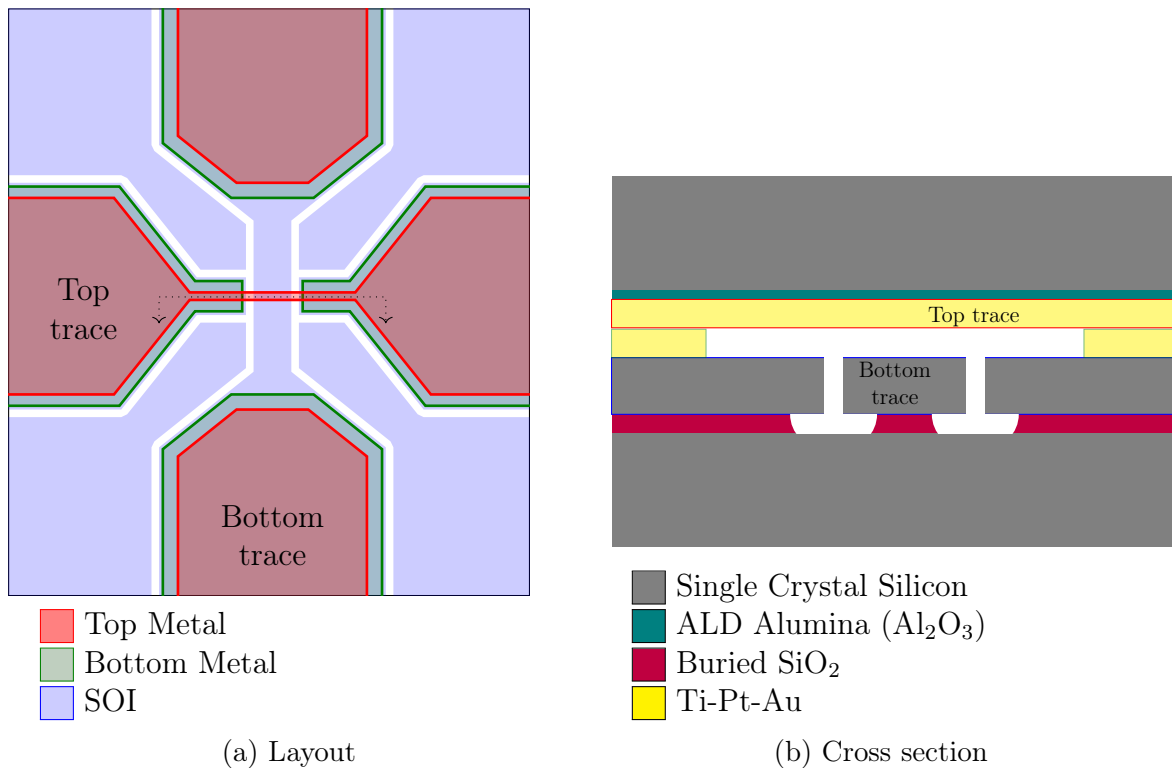
Figure 2.7: Test structure for 2-level routing with bridges. The bridges are tapered to allow for additional misalignment. In fabrication, we produce an array with alignment tolerances from 50 µm to 200 µm .

2.4 Second-generation devices and test structures

For the second generation, more motor variations incorporated learnings from testing the first-generation devices. Given the focus on electrical test structures for two-layer routing in the first generation, that mask was still fabricated with process improvements for electrical testing. This resulted in free space to test different device variations, summarized in Table 2.3.

Figure 2.8: Contact resistance test structure. Four point measurement is done, with current applied across the outer pads and a volte measured across the inner pads. Misalignment in between top and bottom metal keeps the are constant.

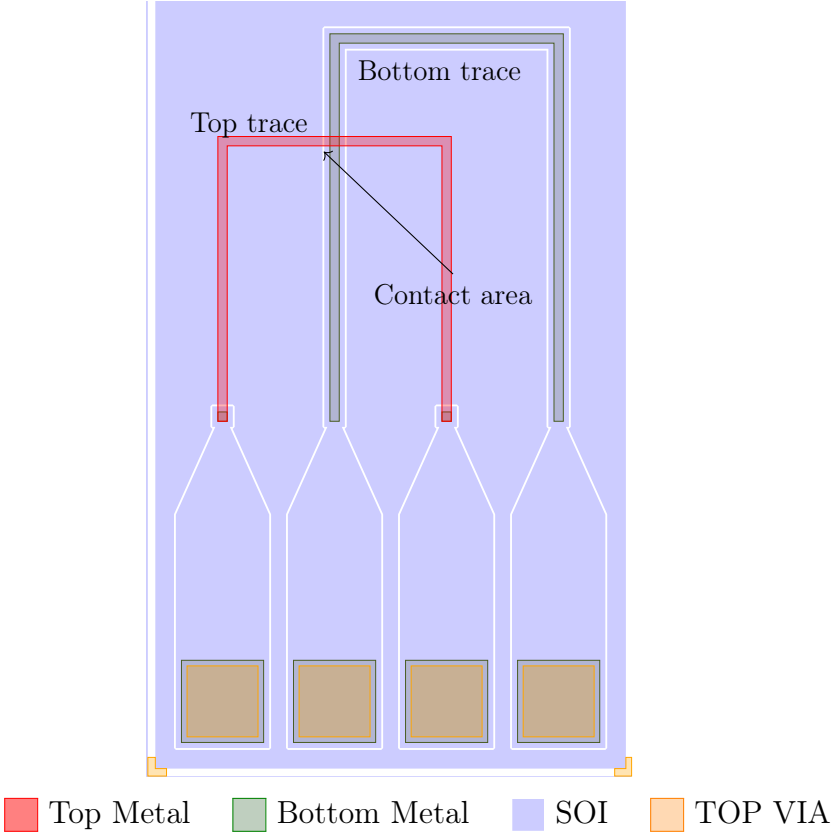Table 2.3: Characteristics of second-generation rotary motors

Parameter	Symbol	2A	2B	2C	2D	2E	2F	2G	2H	Unit
External shuttle radius	$R_{shuttle}$	200	300	500	750	150	200	300	500	µm
Internal shuttle radius	R_{in}	100				200		0	100	µm
Hub type	-	Dimpled	Convex	Convex	2-spring	Convex	Convex	Dimpled	Dimpled	-
Number of fingers per GCA	N	50				60		75		-
Overlap finger length	L_{ol}	70				80		60		µm
Spring length	L_s	260		240						µm
Initial capacitance GCA-A	$C_{GCA}(y=0)$	0.71				0.97		0.91		pF
Maximum capacitance GCA-A	$C_{GCA,\mathrm{max}}$	2.55				3.49		3.27		pF
Spring constant	k_{spr}	12		15.3						kHz
Angled arm length	L_{arm}	129		130		110		114		µm
GCA resonance frequency	f_{res}	10.4		11.8		10.5		10.1		kHz
Pull-in time	$t_{pull-in}$	10.7	10.7	10.7	10.7	10.3	10.3	11	11	µs
Pull-out time	$t_{pull-out,1\mu m}$	362.6	362.6	361.4	361.4	317.4	317.4	421	421	µs
Maximum operation frequency	f_{max}	2.68	2.68	2.69	2.69	3.05	3.05	2.32	2.32	kHz
GCA efficiency	η	23.8%		23.6%		23.8%				-
Output force at 120 V	$F_{x,out}$	1.06		1.05		1.46		1.36		mN
Output torque at 120 V	$T_{GCA,A}$	424	636	1054	1580	437	583	818	1363	nN m
Power at 120 V, 1 kHz	P_{total}	18.33				25.14		23.57		µJ

(a) Dimpled hub

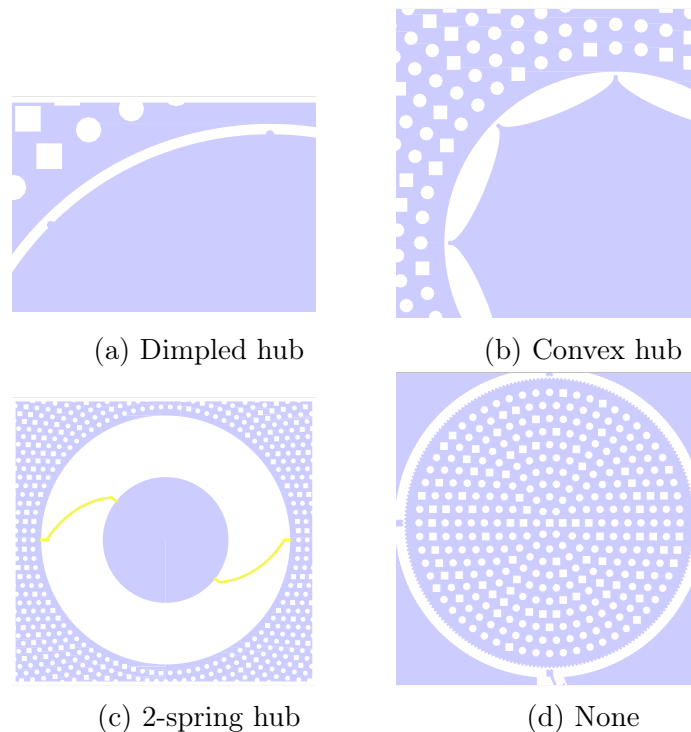(b) Convex hub

(c) 2-spring hub

(d) None

Figure 2.9: Second-generation hub styles: (a) and (b) zoomed in to show dimples and features, respectively; (c) is for torque estimation and (d) uses no central hub at all.

This section explores the design improvements and differences from the first generation. The overarching goals of the second generation of devices were to correct issues preventing proper functionality and testing in the first round, as well as to expand the range of electromechanical characteristics of the motors, including the ability to prevent moisture ingress.

2.4.1 Hub design

In first generation devices, it became obvious that non-symmetric central spring designs resulted on unequal forces in oposing pawls. The only successfull motors of the frist generation were designs 1B and 1C with the spring carefully broken using a probe tip. Even though these motors were able to rotate, lateral displacements of the rotor hubs above $10\,\mu\text{m}$ were observed in the videos.

In the second generation, an internal hub with dimples was introduced, as shown in Figure (2.9) a, such that the central shuttle can displace the minimum feature size of $2\,\mu\text{m}$ at a maximum. This is designed to reduce potential points of friction and additional force.

2.4.2 Triangular fingers

In first generation devices, we observed high leakage currents after closing of GCAs at voltages above 80 V (see section (4.3.1) for more details).

A clever change to the interdigitated capacitor design changes the finger shape to be triangular for stiffer fingers (personal communication, Daniel Teal). Figure (2.10) shows an implementation of the design, based on the following constraints: The front gap is g_1 is kept perpendicular to the direction of motion and at the same value. The overlap length L_{ol} is also preserved. The narrow end of the fingers is determined by the minimum feature in the lithographic process, $2\,\mu m$. The finger is widened as much as posible while preserving the back-gap g_2. The pitch of the fingers, and therefore total area occupied, remains the same.

Assuming parallel plate capacitors on both sides, equation (2.1) is modified to

$$C_{GCA}(y) = \epsilon_0 \epsilon_r Nt \left(\frac{L_{ol}}{g_1 - y} + \frac{L_{ol}/\cos\alpha}{g_2 + y\cos\alpha} \right) \tag{2.7}$$

and the force is therefore given by

$$F_{triang,y} = \epsilon_0 \epsilon_r Nt L_{ol} \left(\frac{1}{(g_1 - y)^2} - \frac{1}{(g_2 + y\cos\alpha)^2} \right),$$

where α is the angle of slated finger side with respect to the horizontal. Ignoring fringe capacitances, to a first degree, the capacitance is a little bit larger than the recangular design. Similarly, the force in the y direction is slightly increased, since the force pulling on the back of the finger is now at an angle. The x components are symmetric and cancel out, and the flexures are very stiff in the x direction by design.

We implemented this concept in all second-generation motors except for 2H and 2G, where we shortened the finger length.
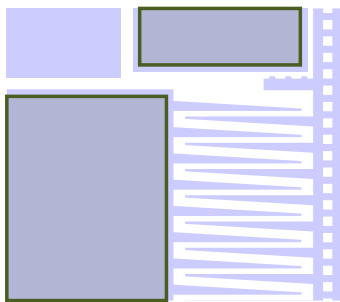

Figure 2.10: Triangular finger implementation. Wider base leads to stiffer fingers. Design concept by Daniel Teal (personal communication).
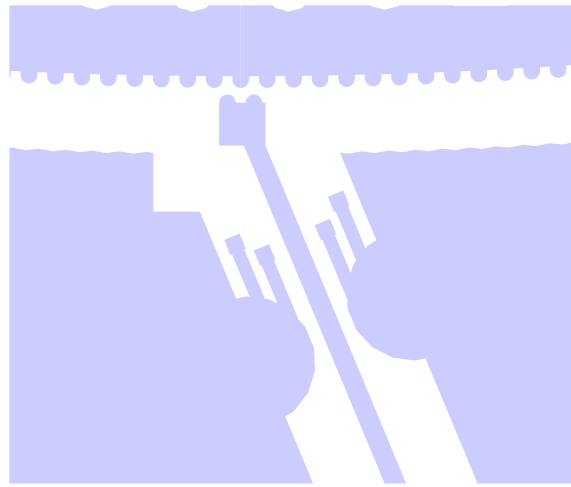
Figure 2.11: Hair-like structures for super hydrophobic surfaces.

2.4.3 Hydrophobic structures

Structures to discourage moisture ingress were added to certain second generation motors, together with test structures to test them . These structures are hair-like, as shown in Figure 2.11. The idea behind these structures is to discourage moisture ingress by increasing the aparent contact angle, similar to super-hydrophobic surfaces [6]. The main risk with such designs is limitation of motion to the angled arm and potential sticking between the parts.

Chapter 3 outlines the fabrication process that was used to fabricate the devices.

Chapter 3

Device Fabrication

3.1 Fabrication overview

The devices in this thesis were fabricated in a process insipired by the standard 3-mask SOI process developed by the Pister group [38], with some significant modifications.

The process was designed with the following considerations. First, building high aspect ratio structures for the gap-closing actuators and inchworm mechanims is needed. Moreover, the structures must be covered and protected from the aqueous environment for proper motor functioning. However, a part of the mechanism is needed to interface with the fluid; a hermetic seal is not appropriate if the flagellum must be in contact with the water. Therefore, a process similar to the one used by Erasmis [10] was chosen, but enabling an out-of-plane mechanical feedthrough for the flagellum. A silicon wafer was used the lid because it allows high-aspect ratio, lithographically defined, etching of through-wafer vias. Glass wafers, on the other hand, cannot be etched with high aspect ratios, to the best of this author's knowledge.

First an overview of the fabrication steps is provided, with details on each step further in this chapter.

The bottom wafer (Figure (3.1)) is a SOI wafer with a device layer thickness of 40 µm, 550-600 µm handle thickness and a 2-3 µm burried oxide. The thickness variation is a function of wafer availability at the time of fabrication and should not affect device preformance.

A Ti-Pt-Au metal stack with a lift-off technique was deposited, with a 20 nm titanium adhesion layer, a 20 nm platinum diffusion barrier, and a 750 nm gold layer for bonding, wire bonding, and electrical conductivity. Then, DRIE 40 µm deep was used to define the features of the SOI layer. This layer includes all the mechanical moving parts, defined by appropriately spaced etch-holes for release after bonding.

On a separate, 350 µm, silicon wafer (Figure (3.2)), a layer of alumina (AL_2O_3) via atomic layer deposition (ALD) was added. This is followed by the same metal stack used for the SOI wafer. Subsequently, the alumina is pattern and etched, followed by a through-wafer DRIE.
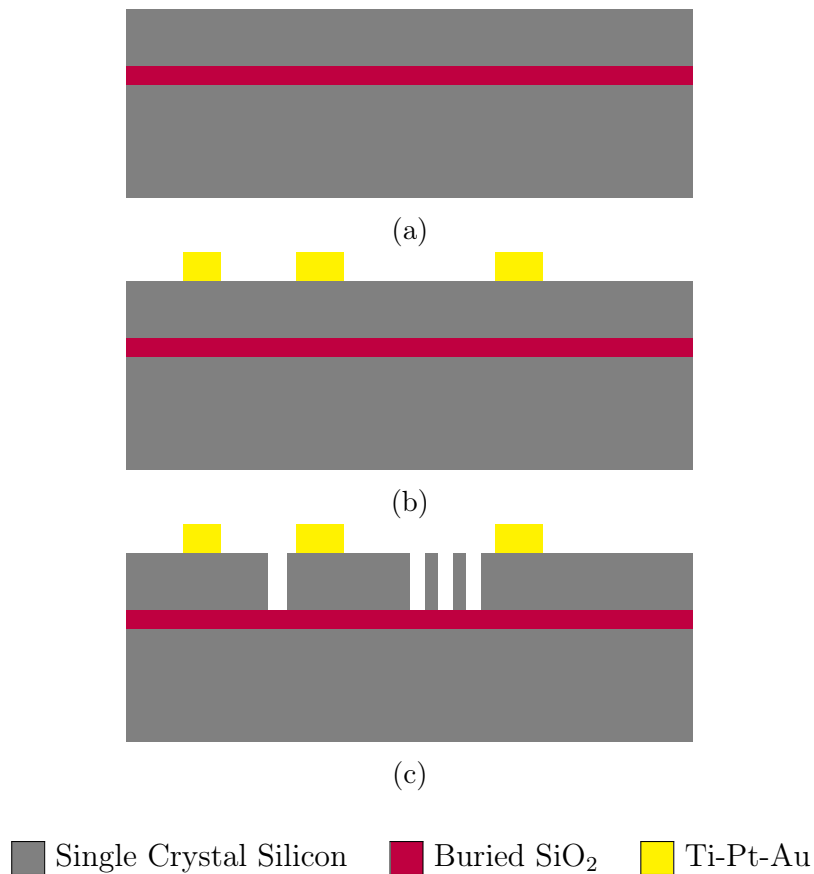
Figure 3.1: SOI wafer fabrication process: (a) SOI wafer with 550-600 µm handle, 2-3 µm buried oxide, and 40 µm SOI layer, (b) Ti-Pt-Au (20-20-750 nm) evaporation and liftoff, (c) 40 µm DRIE etching.

The devices are then bonded with gold-gold thermocompression bonding, singulated, and released in vapor HF, as shown in Figure (3.3). Two different versions of the process were used for thermocompression bonding and singulation. In the first case, the wafers are cleaned, bonded together, and then diced. In the second version, both wafers are diced, and the chips are individually cleaned and bonded. See Section(3.4.1) for a detailed discussion of each bonding procedure and its relative advantages.

Then, a hydrophobic coating is applied using a self assembled monolayer (SAM) to increase the contact angle with water. Figure (3.4) shows the desired effect on hydrophobic coating on these devices.

Finally, an artificial flagellum must be attached. For this proof-of-concept device, spiral wire bond to the shuttle was used, but current 3D printing technology and 2-photon lithography allow for the creation of spirals at the appropriate length scale [2].

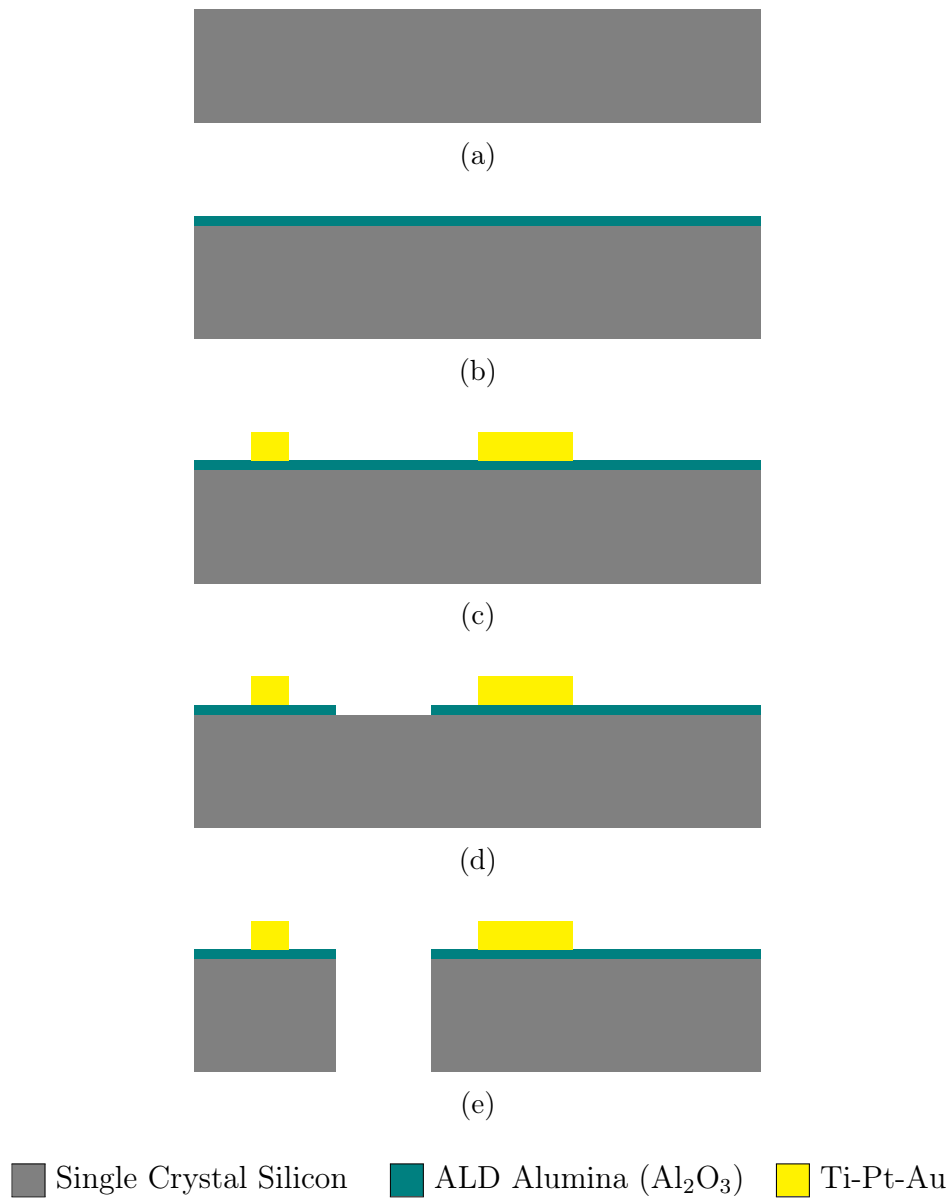Figure 3.2: Top wafer process flow: (a) bare $350\,\mu m$ wafer, (b) $100\,nm$ ALD alumina (Al_2O_3), (c) Ti-Pt-Au e-beam evaporation (d) alumina etch, and (e) through wafer DRIE.

(a)

(b)

(c)

■ Single Crystal Silicon ■ ALD Alumina (Al$_2$O$_3$) ■ Buried SiO$_2$ ■ Ti-Pt-Au
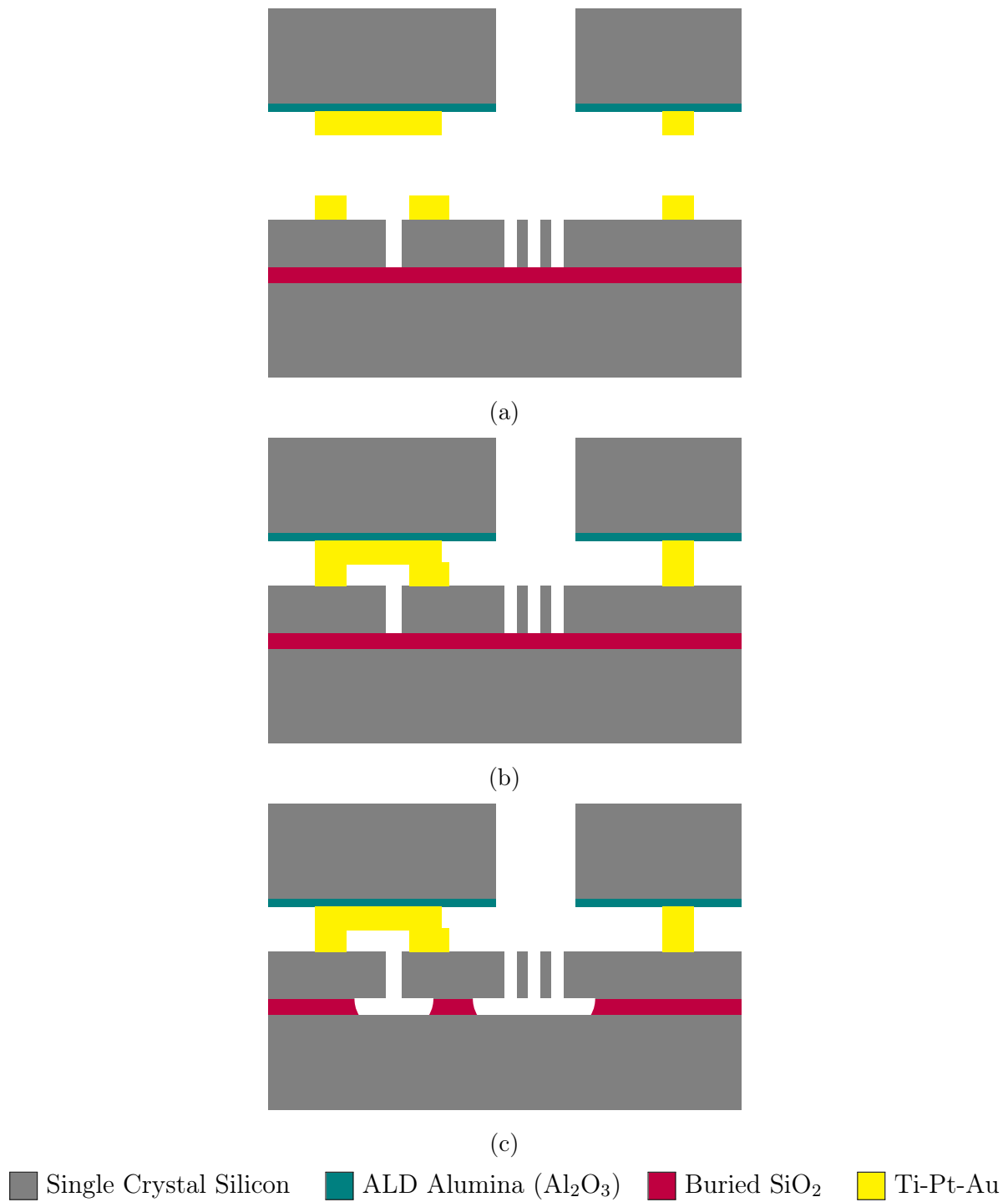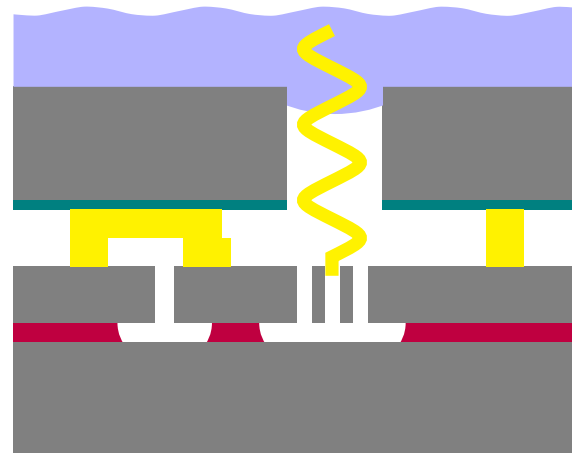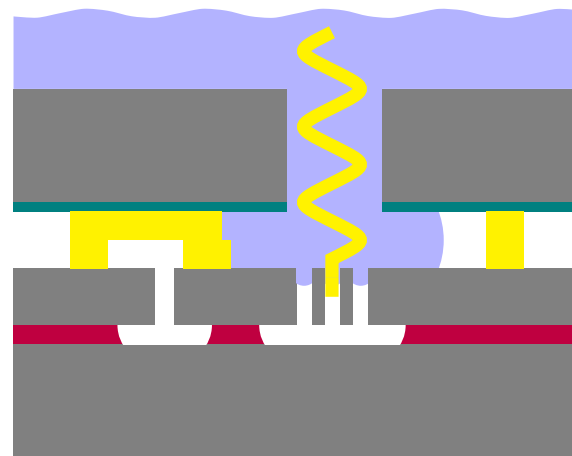
Figure 3.3: Bonding and release: (a) devices are aligned, (b) thermocompression bonded, and (c) released in vapor HF.

(a)

(b)

Figure 3.4: Final fabrication step: Hydrophobic SAM coating, attachment of artificial flagellum. Two different configurations of hydrophobic coating: a) air-water interface at through-wafer via, (b) air-water interface at smaller gaps.

3.2   Fabrication: 1st and 2nd generation

The design and fabrication process consisted of two phases, which are referred to as first-and second-generation devices.

The first generation fabrication goal was to demonstrate the feasibility of gold-gold bonding as a packaging solution for this application, testing the basic functionality of the devices and two wiring layers and the achievable fabrication and alignment tolerances.

The results of the first generation informed several changes in the second generation fabrication. The SOI wafers used in the first generation were doped to a resistivity of $1\text{-}25\,\Omega \cdot \text{cm}$. The electrical measurement of the traces on this device showed an unwanted rectifying behavior on the metal-semiconductor surface (see Section (4.2)). To address this, in the second generation SOI wafers rated below $10\,\text{m}\Omega \cdot \text{cm}$ were used. Due to supply limitations, changing the handle wafer from $550\,\mu\text{m}$ to $600\,\mu\text{m}$ was required as well as changing the thickness of the buried oxide from $2\,\mu\text{m}$ to $3\,\mu\text{m}$. The SOI layer thickness was maintained to keep the important electromechanical charactersitics and reuse the well-tuned DRIE recipe.

Additionally, fabrication improvements between generations included more careful and thorough cleaning and handling for effective wafer bonding.

3.3   Through-wafer DRIE

Vias through the top wafer are necessary for the flagella to contact water and to probe or wire bond for electrical connection.

For through-wafer etching, $12\,\mu\text{m}$ of AZ12xT photoresist, manually spun and hard baked for 30 minutes at $120\,^{\circ}\text{C}$. The selectivity of photoresist during the DRIE etch depends on the thermal conditions of the etch. A handle wafer is required to protect the platen when etching through the hole wafer, which results in heating of the photoresist and poor selectivity.

Experimentally, it appears that all $12\,\mu\text{m}$ of photoresist is etched if all 350 µm of silicon were etched with a handle wafer. To solve this issue, the etch was completed in two steps: first, the vias are etched into the chamber in a timed DRIE etch of around 200 µm. The wafer was then bonded to a mobile electrostatic chuck (Eshylon Apache) and the etch is completed. Because the whole wafer is etched, it is easy to visually verify completion of the etch.

3.4   Gold thermocompression bonding

Thermocompression bonding consists of the application of heat and pressure to two wafers in contact [46].

Gold-gold thermocompression bonding was selected because it is widely used in semiconductor packaging. Gold is a desirable material because it is conductive, resistant to corrosion, and does not form an oxide [46]. This last characteristic facilitates diffusion of the metal surfaces in contact.

For gold thermo-compression bonding, the temperatures must be kept below the Si-Au eutectic point of $363\,°C$ to prevent diffusion of silicon into the gold layer. As an additional safeguard, $20\,nm$ of platinum below the gold layer was included, which acts as a diffusion barrier.

3.4.1   Wafer and flip-chip bonding

Two different bonding and singulating procedures were used successfully. Selecting the best strategy depends on the desired alginment tolerance, the need for processing in parallel, and the available tools.

Two different bonding setups were available: an AML AWB-08 wafer bonder and a Finetech FINEPLACER 96 Lambda flipchip bonder.

In initial versions of the process, bonding at a die level allowed several attempts with different bonding conditions and cleaning procedures. Moreover, the likelihood of particle contamination preventing a successful bond is smaller over the smaller die than across the whole wafer.

However, this process has several limitations. First, the configuration of the Fineplacer 96 Lambda, used here, can apply up to $20\,N$, which limits the gold contact area to $6.7 \times 10^{-7}\,m^2$ in order to apply the $30\,MPa$ which results in successful bonding. Another limiting factor for the flip-chip bonder is that the heaters cannot be on for longer than 5 minutes. As a work around, the chips with the flip-chip bonder were partially aligned and bonded and then, the AML AWB-08 bonder was used to apply higher forces. For individual bonding, the die must first be singulated. The most sensitive structures, such as springs and angled arms, would often break during the dicing process (Figure (3.5)).
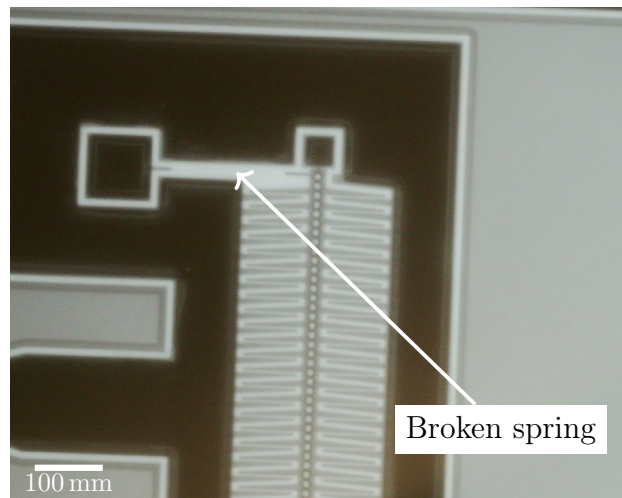

$100\,mm$

Broken spring

Figure 3.5: Broken spring during dicing.

Solutions to this include carefully cleaving the wafer along crystal planes — which requires good angle alingment to the wafer flat during lithography steps — and protecting the structures with another layer of dicing tape on top.

Although wafer bonding is more difficult to achieve, it leads to better results. The benefits of wafer bonding include higher throughput and a cleaner bonding environment. This is because the available flip-chip bonder is not in a well-filtered cleanroom, where as the wafer bonder is in an innert environment. Moreover, the wafer bonder is set up for high vacuum, so it could be bonded below 10^{-6} Torr. The configuration of the AML AWB-08 allows forces up to $25\,\mathrm{kN}$. To apply $30\,\mathrm{MPa}$, this limits the gold-gold contact area to $8.3 \times 10^{-4}\,\mathrm{m}^2$ or approximately 4.6% of the wafer area. Dicing after successful bonding is more reliable, because the top wafer keeps the protects sensitive structures(see Figure (3.5)).

3.4.2 Factors affecting succesful bonds

Succesful gold-gold bonding is key to the electrical and mechanical operation of the devices. Electrically, the bonds act as interconnects between the metal on the top and bottom wafer, enabling an additional layer of routing. Quality bonding is also important mechanically, as the top wafer prevents the released structures from falling out of plane and keeps the gap-closing actuator structures dry. The mechanical integrity of the bond is also important in the fabrication of robust microswimmers.

Metal topography

A fundamental aspect of a good bond is that the metal layers in contact are flat. Uneaven metal layers, stringers, and adhesion issues present the same problem as particles — they prevent most of the desired bonding areas from coming into contact.

Ensuring a clean, stringer-free, lift-off process was critical to bonding success. Here, stringers refer to metal portruding outside away from the wafer surface due to some vertical sidewall coverage.

In general, lift-off processes work by patterning photoresist and subsequently sputtering or evaporating a metal, and removing the photoresist with all the metal above it. Ideal lift-off requires a discontinuity between the metal layer on the substrate and the photoresist. For thin layers deposited directionally (such as by evaporation), this can often be achieved with a standard photoroesist. However, since a relatively thick layer of gold was needed, a lift-off resist (LOR 5A) was used. LOR 5A is not photosensitive, but it etches isotropically in photoresist developer. Thus, the developing step can be tied to produce an undercut beneath the photoresist. Figure (3.6) shows a lift-off process with LOR. Note that, even if the deposition is not perfectly perpendicular to the wafer or some sidewall coverage exists, a discontinuity can be guaranteed. The manufacturer recommends that the thickness of the metal stack do not exceed two thirds of the LOR thickness. If the LOR layer is too thin (or nonexistent), any coverage of the sidewalls might remain during the photoresist removal

step, which are hereto refered as stringers. Figure (3.6b) shows the effects of stringers, as well as the adhesion problems when stringers pull part of the metal off the substrate.

Details of metal evaporation

The Ti-Pt-Au evaporation was done in an e-beam evaporator (CHA Solution). Since $1\,\mu m$ is a relatively thick layer of Au, the evaporation takes a long time. When evaporating below $3\,\text{Å/s}$, flakes of Au were deposited in the chamber.

This is likely due to the radiative heating of the photoresist in the vacuum chamber. An evaporation rate of 5Å/s resulted in no flaking. Although higher rates of evaporation require more energy, it reduces the amount of time the photoresist is exposed to the glowing hot crucible.
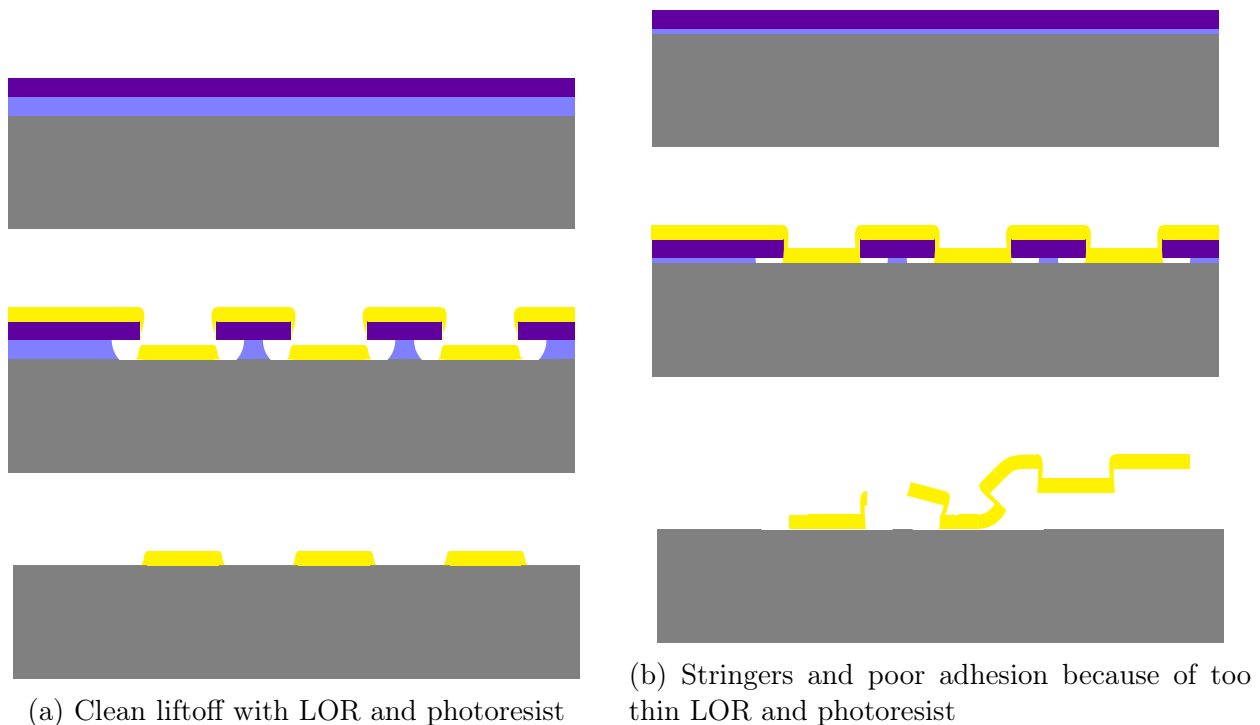

(a) Clean liftoff with LOR and photoresist

(b) Stringers and poor adhesion because of too thin LOR and photoresist

Figure 3.6: Lift-off process with LOR.

3.4.3   Bonding alignment

Regardless of the bonding method used, bondign alignment limits miniaturization, since large missalignments would result in unwanted shorting and gaps in this hermetic seal with a mechanical feedthrough. There are several factors that affect the final alignment.

Optical clarity

Both tools available for bonding use optical methods for alignment. In the case of the wafer bonder, in practice infrared alignment was limited when the wafers used were not double-side polished (resulting in unnecesary difraction and bluring). This was not an issue when flip-chip bonding.

Platen alignment

If the bonding platens are not parallel, the wafers (or chips) shift during bonding. Figure (3.7) shows the mechanism that leads to this.

A similar problem occurs when the flip-chip bonder is used for chips that are too large (such that they don't appear parallel as they are brought closer), or if the height of the lower platten is not properly aligned. These problems can be likely mitigated with proper calibration of the flip-chip bonder.
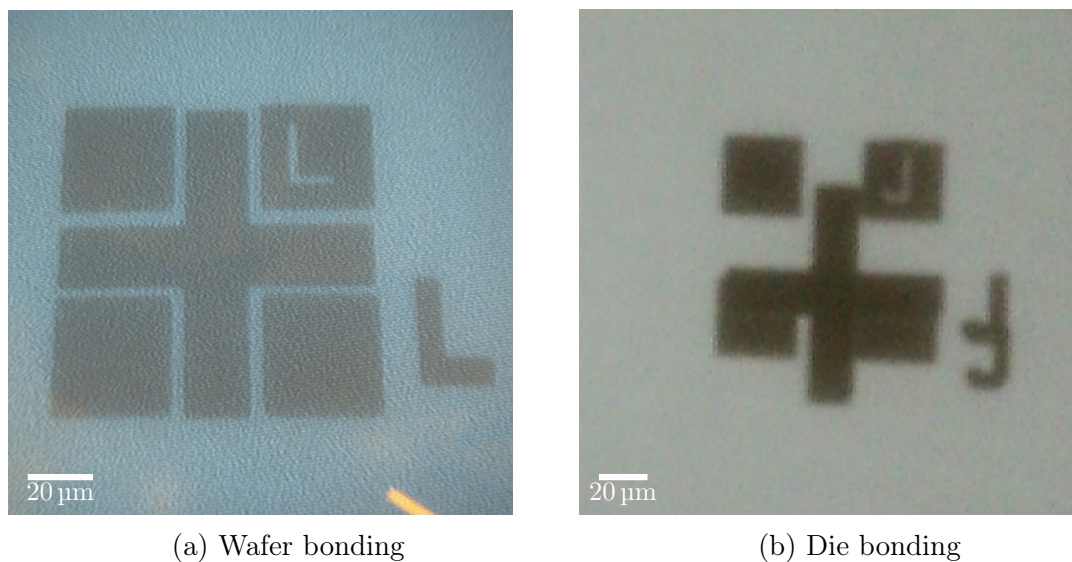

| (a) Wafer bonding | (b) Die bonding |

Figure 3.8: Alignment for wafer and flip-chip bonding, taken with IR microscope. Wafer bonding alignment is within $2\,\mu m$ whereas we only achieved around $18\,\mu m$ for die bonding.

Figure (3.8) shows the alignment achieved after flip-chip and wafer-level bonding. Sub-$2\,\mu m$ alignment was achieved using the wafer bonder and $18\,\mu m$ using the die bonder.

3.5 HF release of bonded chips

The chips were released in anhydrous hydroflouric acid (Figure (3.3c)) using a Primaxx uEtch (SPTS). Anhydrous HF is used to prevent stiction compared to wet HF etches, but generally
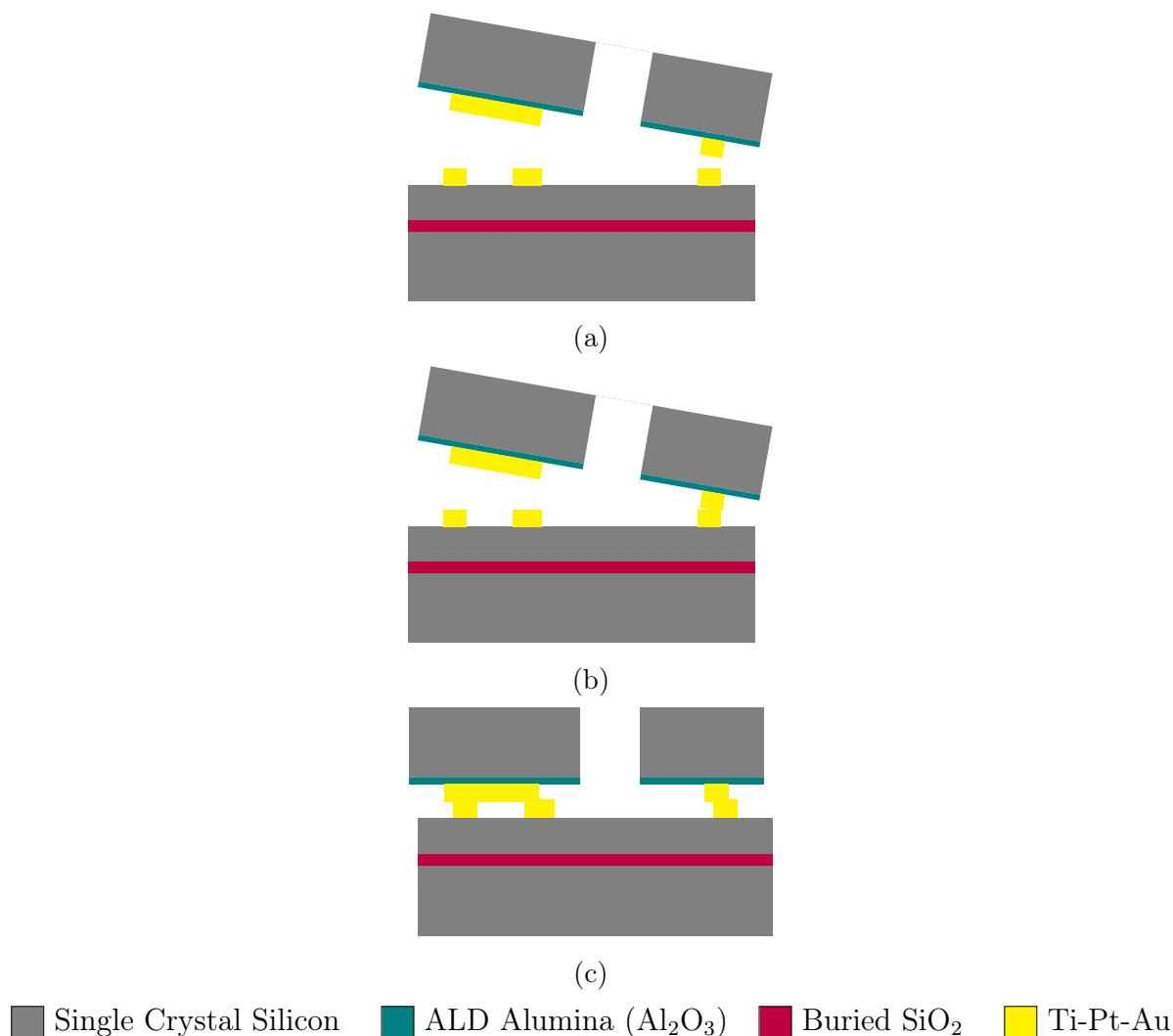
Figure 3.7: Bonding misalignment due to non-parallel platens. The wafers (a) are aligned optically, (b) then brought into contact, which then results in (c) sliding and final misalignment.

has a lower etch rate [23]. Vapor HF etching is based on a flowing gaseous hydroflouric acid together with ethanol (or another alcohol) and nitrogen gas. The purpose of alcohol is to remove by-products of the silicon oxide and HF reaction and to prevent the formation of liquid water.

In previous designs, the moving structures were easily exposed to the process gases, which need to diffuse through the etch holes and, at a maximum, the undercut distance. Therefore, in the case of uncapped devices, the gasses necessary for the etch process are not diffusion-limited: at the fastest etch rate (recipe 5 in Table 3.1), the devices were released without
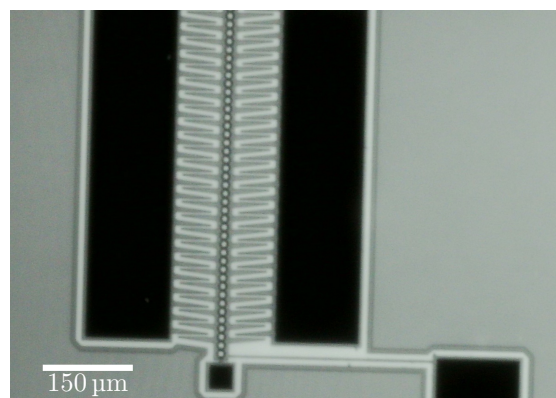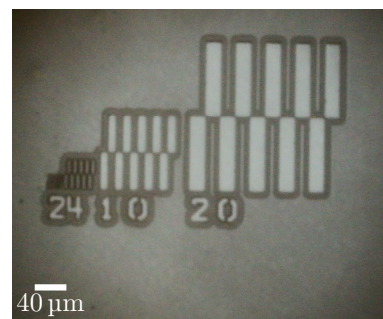
(a) Unbonded, fast etch rate
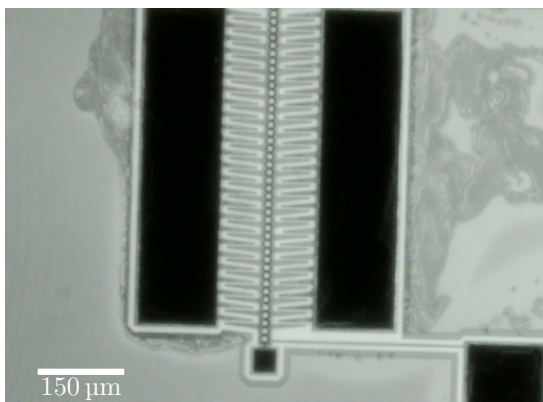
(b) Bonded, fast etch rate
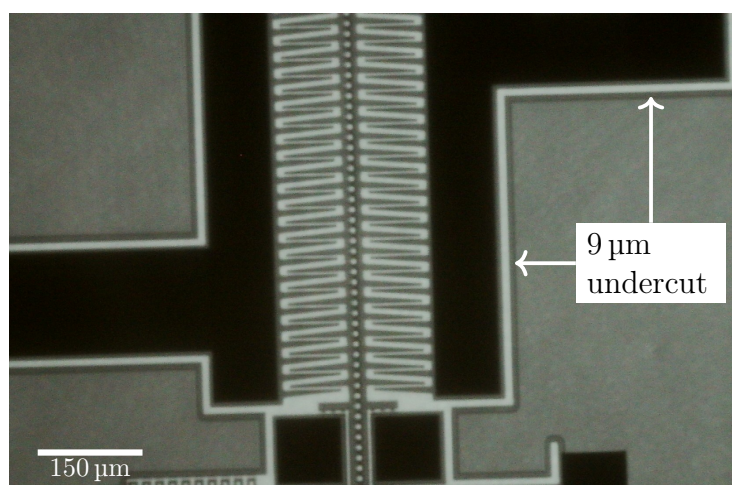
(c) Bonded, slow etch rate

(d) Bonded, slow etch rate test structures

Figure 3.9: Oxide release in vapor HF: a) fast etch rates work well when unbonded, b) when bonded, faster etch rates (recipe 5 in Table 3.1) result liquid HF formation and uncontrolled etch rates. However, c) slower etch rates (recipe 2) work well when bonded. All etches were timed to achieve 8-10 µm undercut.

issues.

However, when the same recipe was used for bonded devices, the etch rates were highly uneven because of the formation of liquid water, and therefore liquid HF, in certain areas. This results in much higher, "race away" etches in certain areas, as depicted in Figure (3.9b). However, a higher ratio of ethanol to vapor HF results in slower etch rates and a lower liquilihood of liquid HF generation. Data from a recent study indicates that vapor HF is a viable release mechanism without major stiction issues even at extremely high aspect ratios [14].

Recipe number	Nominal etch rate (nm/min)	N_2 (sccm)	Ethanol (sccm)	HF (sccm)
2	36	1250	350	310
5	130	880	325	720

Table 3.1: Vapor HF etch step gasses. Adapted from Marvell Nanofabrication Laboratory process manual.

During the development and testing of these devices, only a few chips were released at a time. However, given the low etch rates necessary to prevent "race away" undercuts, fully releasing the die can take over 7 hours, making it expensive and inconvenient. One workaround explored with mild success was"pre-releasing" the devices before wafer-level bonding, followed by bonding, dicing, and a final release step. The first HF release was timed to achieve an undercut of 1-2 μm, so most structures remain anchored to the substrate. After this, single chips can be etched for the remaining undercut until all the devices, designed with a release length of 8 μm, are released. This strategy worked well for certain devices. However, narrow serpentine springs (<2 μm) did get stuck during the dicing process, when water is inevitably introduced. Ultimately, these efforts advise against this strategy to ensure higher yield.

3.6   Wafer dicing and singulation

The devices were singulated by scoring them with a Disco DAD3240 automatic dicing saw. The whole stack up includes a 643 μm SOI wafer, 1.5 μm metal stack, and 350 μm top wafer. The total wafer stack is about 1 mm thick.

The blade height was set such that it cuts 700 μm into the wafers, completely cutting through the top wafer and only partially cutting through the SOI wafer. Manual application of gentle pressure then breaks the bottom wafer along the weaker dicing lanes. This allows for use of dicing blades with 0.9 mm exposure.

Afterward, the wafers were expanded with a Dynatex DXE-5 die expander. This prevents chipping of the devices while separating them from the dicing tape.

Strong bonds are necessary for proper dicing — when the devices were weakly bonded, the shear forces and water spray during the dicing process stripped the top wafer appart. Thus, the dicing process serves as a preliminary bond strength test for these devices. See Section (4.2) for a detailed description of the results.

3.7   Hydrophobic coating

As discussed in Chapter 1, a hydrophobic coating is critical to preventing water ingress through small gaps. Two options were considered for hydrophobic coating: a PECVD flouropolymer and a self-assembled monolayer (SAM).
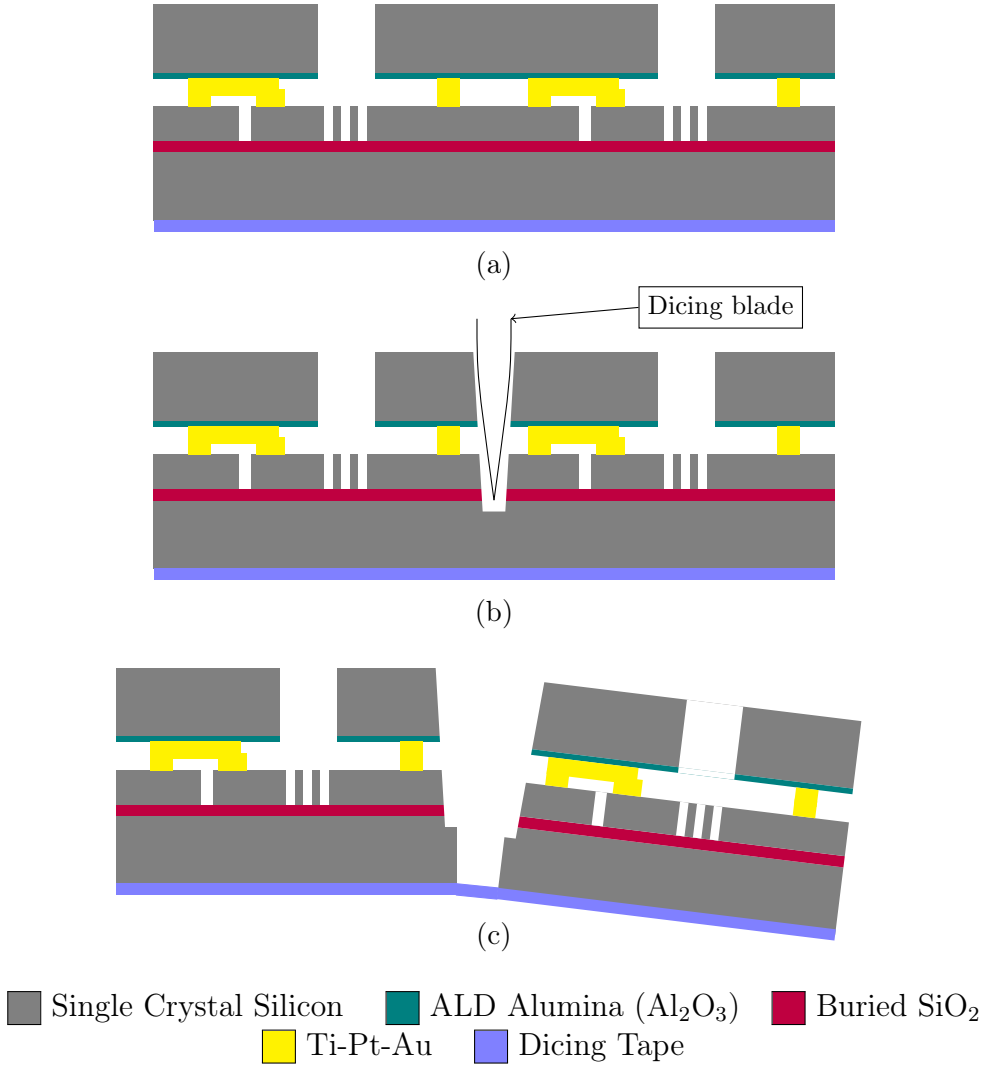
Figure 3.10: Singulation process: (a) bonded wafer on dicing tape, (b) partial dicing with wafer saw, and (c) breaking of chips and die-expansion.

To quantify hydrophobicity, the contact angle of a sessile droplet can be measured. Primary experiments showed the flouropolymer can achieve a contact angle of 103- 110°, depending on deposition parameters. PECVD flouropolymer layers were deposited in a Plasma-Therm PK-12 RIE chamber plumbed with C_4F_8, with recipes based on [45]. Table 3.2 shows

| Treatement	Pre-treatment CA	Post-treatment CA
PECVD Flouropolymer 60 sccm C_4F_8 60 mTorr 100 W 60 s	63.7°	110°
PECVD Flouropolymer 60 sccm C_4F_8 60 mTorr 100 W 90 s	63.6°	107°
PECVD Flouropolymer 60 sccm C_4F_8 60 mTorr 100 W 30 s	62.2°	105.6°
PECVD Flouropolymer 60 sccm C_4F_8 58 mTorr 125 W 60 s	38.89°	106.7°
PECVD Flouropolymer 60 sccm C_4F_8 76 mTorr 100 W 120 s	-	104.4°
PECVD Flouropolymer 30 sccm C_4F_8 30 sccmCF_4 60 mTorr 100 W 120 s	-	105.1°
PECVD Flouropolymer 30 sccm C_4F_8 15 sccmCF_4 78.5 mTorr 100 W 120 s	-	103.4°
Silane SAM 50 W 15 s plasma clean. 20 min silane exposure	-	105.5°
Silane SAM 50 W 15 s plasma clean. 20 min silane exposure	-	109.06°

Table 3.2: Contact angle, before and after PECVD Flouropolymer and trichlorosilane Self Assembled Monolayer (SAM).

the results of different flouropolymer recipes.

Another alternative is a silane self-assembled monolayer (SAM), using the process described in [19]. Starting with clean chips, 15-30 s of plasma treatment at 50 W were done to functionalize the surface for the silane groups. The chips are then placed in vacuum (28 inHg) for 20 minutes next to a vial with 40 µL of (heptadecafluoro-1,1,2,2-tetrahydrodecyl)trichlorosilane (Gelest SIH5841.0) [1]. This silane precursor was selected over other silane precursors because it was readily available. The silane precursor evaporates and attaches to the surfaces of these devices that were previously functionalized during plasma cleaning. Figure 3.11 shows contact angle measurements after silane treatment on bare silicon and and Al_2O_3, the two materials covering most of the surface area. If surfaces made

---

[1]I'd like to thank Jasmine Jan, who developed and trained on this process.

of additional materials need to be made hydrophobic, a seed layer of Al_2O_3 can be used for better adhesion [17]. Furthermore, there is evidence in the literature that (heptadecafluoro-1,1,2,2-tetrahydrodecyl) trichlorosilane also attaches well to SiO_2.
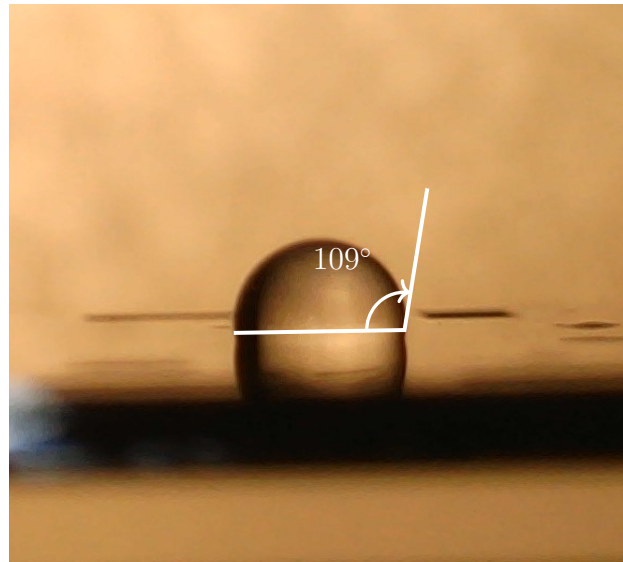
(a) on silicon
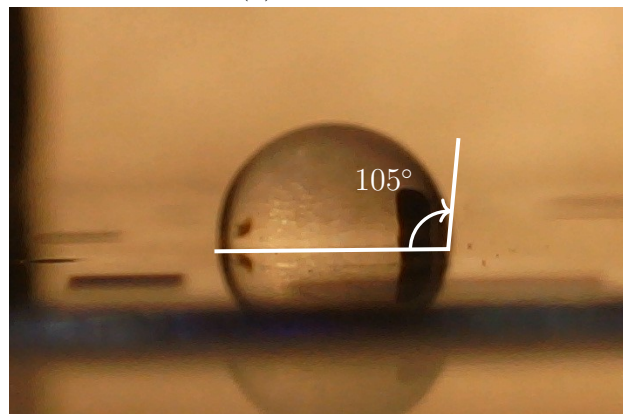
(b) on Al_2O_3

Figure 3.11: Contact angle measurments of water on silicon and aluminum oxide.

In the final process flow, the Silane SAM process was used, due to its simplicity and better reliability.

3.8   Wire bonded flagella

There is significant precedent in the literature on the fabrication of helical artificial flagella. Several microfabrication methods using residual stress to coil a lithographically designed flagellum have been demonstrated [48]. Alternatively, there are several techniques to 3D print appropriate helices [11]. A very effective method of doing so is two-photon polymerazation, which achieves single micrometer hellical diameters [34, 18]. To build useful microswimmers, 3D printing flagella with controls over thickness and wavelength need to be fabricated. However, a useful technique in the initial stages presented in this dissertation involves the use of a wire bonder to create artificial flagella and attach them to silicon. This has the benefit of not requiring 2-photon lithography systems unavailable to us, just widely available wirebonders that are already a part of standard semiconductor packaging.
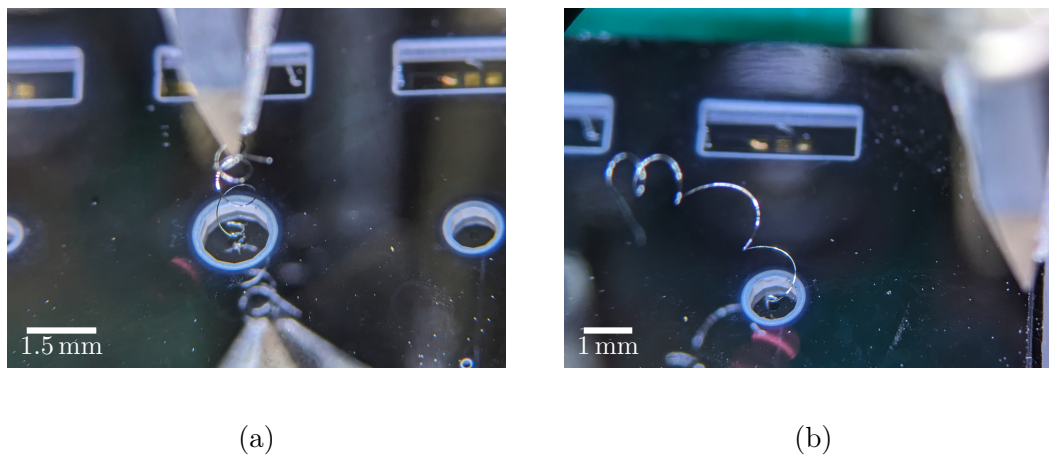

(a)   (b)

Figure 3.12: Wire bond flagella attached to SOI rotors. Through silicon vias are of $960\,\mu m$ for (a) and $1450\,\mu m$ for (b).

A West Bond Model 7400B Wirebonder was used with $25\,\mu m$ diameter silver wire. Forming the coils requires considerable skill: by first rethreading the wire bonder tip. Then, the wire was coild around a wider, circular cross section wire to form a spiral. This was followed by removing the "mold" wire and carefully rewinding the coil to the wirebonder tip. The wirebond flagella is subsequently attached to the SOI silicon like a typical wire bond. Typical results from this type of procedure are shown in Figure (3.12).

This process has some clear limitations. There is a wide variation depending on user skills, making no flagellum the same as the other. Moreover, the helical radius could not be smaller than about $100\,\mu m$. More importantly, the wire bond wedge is too large to wire bond inside any through-hole vias below approximately $500\,\mu m$ in diameter.

There are two potential solutions to work around this limitation. First, the flagella can be wire-bonded prior to die-level bonding, ensuring it is properly threaded through the silicon via when bonding. This is possible but likely challenging. Alternatively, modifying the

process so that the cap wafer is thinner (or the SOI layer of a wafer) could help create small vias that do not require such a high aspect ratio. This also has the benefit of significantly reducing the device mass.

Chapter 4

Results

This chapter discusses the performance of the devices in this dissertation. In summary, it was possible to demonstrate fast speeds during dry operation, the effect of hydrophobic coating on moisture ingress as seen in the electrical characteristics.

This chapter aims to describe the test setup, survey the data collected, and summerize the lessons that can be derived from it.

4.1   Test Setup

These devices were tested by collecting electrical and optical data of operation simultaneously at a probe station. With this setup, the electrical characteristics of the motors can be accurately mapped to their mechanical operation.

4.1.1   Electrical testing

The devices were driven by the circuit shown in Figure (4.1). The circuit consists of an Arduino drives the gate of two NMOS transitors (one for GCA-A and one for GCA-B) with a pull-up resistor. This enables low-voltage control of high voltage (35 V - 120 V) signals used to drive the GCA.

The power supply voltage V_{DD} was set during device operation to modulate the amplitude of the square waves $V_{in,A}$ and $V_{in,B}$ that drive the two sets of GCAs. To estimate power consumption of the devices, a known resistor R_{meas} was inserted in the return path. The current flowing through the motor is directly proportional to V_{Rmes}. An oscilloscope was used to collect the wave forms $V_{in,A}$ and V_{Rmes}, as well as the trigger signal suppiled by the Arduino.

Figure (4.2) shows an example of the electrical data collected during each trial. Recall the mode of operation: when $V_{arduino}$ is high, the GCA-A disengage, and they reengage when $V_{arduino}$ goes low again. $V_{in,A}$ is an inverted version of $V_{arduino}$, but also shows charging and discharging time constants. Finally, there are two peaks in I_{out}. The first is a positive rush
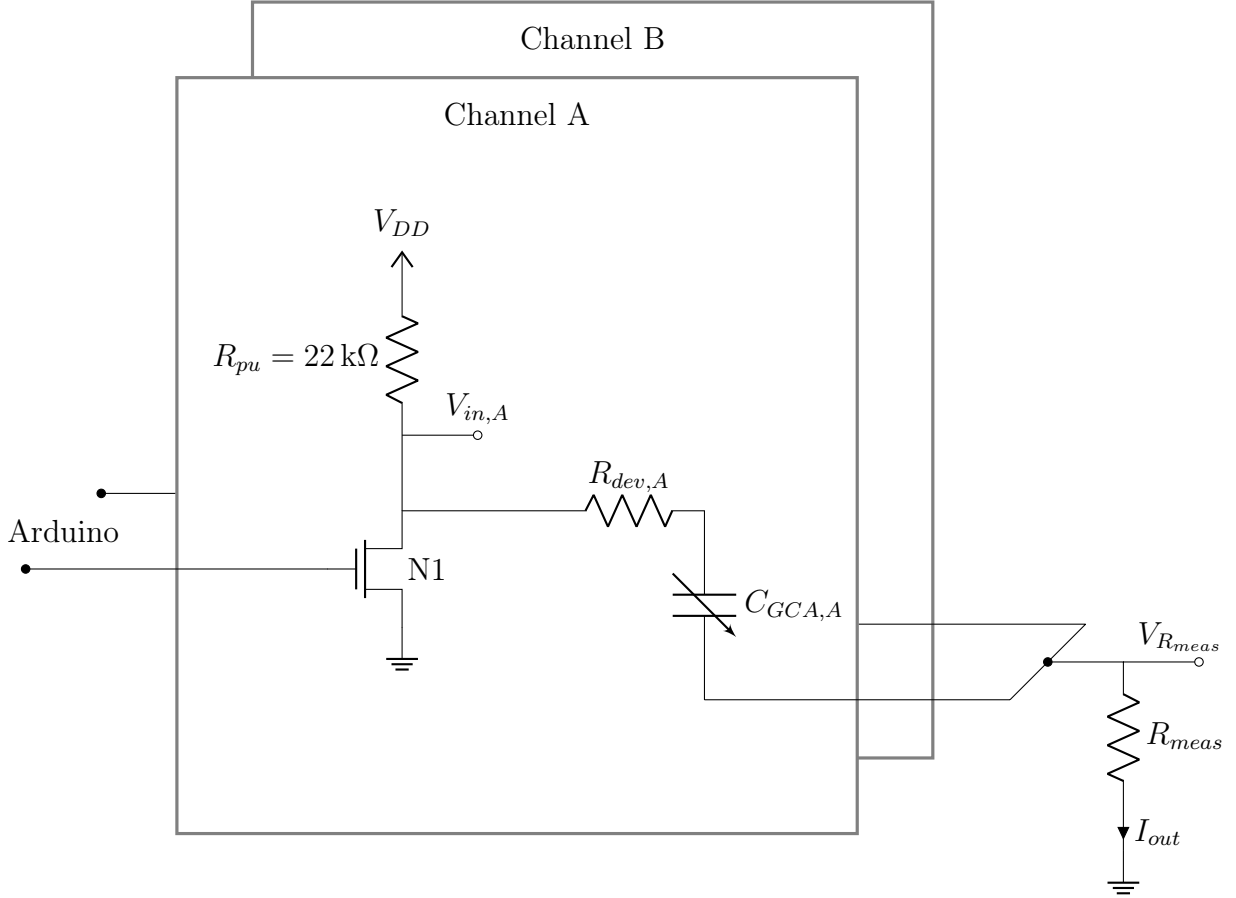
Figure 4.1: Motor driver and measurment circuit. Oscilloscope probes connected at $V_{in,A}$ for voltage measurment on channel A, $V_{R,mes}$ for total current measurement, and the Arduino control signals for triggering. The MEMS devices are abstracted as R_{dev} and C_{GCA}.

of current to charge the GCA capacitors. The second represents a negative flow of current to discharge them.

Recall the capacticance of the GCA as a function of displacement y:

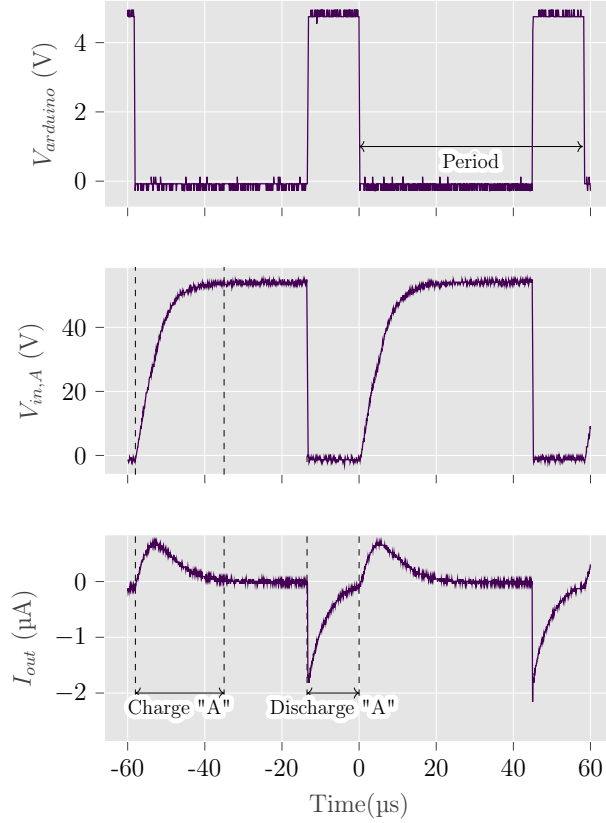$$C_{GCA} = \epsilon_0 \epsilon_r N t L_{OL} \left(\frac{1}{g_1 - y} + \frac{1}{g_2 + y} \right). \tag{4.1}$$

Figure 4.2: Typical electrical waveforms while driving a single set of pawls on a device. $V_{arduino}$ is supplied as the controling signal by the Arduino, $V_{in,A}$ is the voltage curve suplied by the device and I_{out} is the current flowing through R_{mes}.

The current across this capacitor is given by

$$i_{GCA} = \frac{dQ}{dt} \tag{4.2}$$

$$= \frac{d(C_{GCA}V)}{dt} \tag{4.3}$$

$$= \frac{dC_{GCA}}{dt}V + C_{GCA}\frac{dV}{dt} \tag{4.4}$$

$$= \frac{dC_{GCA}}{dy}\frac{dy}{dt}V + C_{GCA}\frac{dV}{dt} \tag{4.5}$$

$$= i_{motion} + i_{elec} \tag{4.6}$$

where $\frac{dy}{dt}$ is the velocity of the gap-closing array. The first term in equation (4.5) can be ignored if the gap-closing actuator is fully closed or stuck, with capacitance changing only due to the second term.

Because the position of the GCA y is a function of the force and the voltage, a full solution of this system requires the coupling of electrical and mechanical components. This work does not present the full solution but approximates it as an RC circuit with a changing time constant.

For a simple RC ciruit, the charging due to a step in voltage is

$$V(t) = V_{max} \left(1 - e^{-\frac{t}{RC}} \right)$$

$$i(t) = \frac{V_{max}}{R} e^{-\frac{t}{RC}}$$

As a simplification, the dominant RC time constant $\tau = RC$ can be computed from the electrical data. Changes in this behavior between the beginning and end of a charging or discharging period are a combination of variations in capacitance as the device actuatuates and the effect of i_{motion} in the charging behavior of the circuits. However, changes introduced by adding a fluid show that water has entered GCA gaps. If R is high (which happens in the first-generation devices and is enforced in the second generation devices by picking R_{meas}), the device capitance in these circuits can be approximated.

Throught this chapter, different characteristics of the signals and their connection to device performance will be referred.

4.1.2 Optical data and video processing

During electrical data collection, video of the devices was recorded using a microscope camera. As will be seen, qualitative observation of these videos and hands-on testing provides useful insight for the MEMS designer. However, a more quantitative analysis requires a systematic way of converting the videos into data on the motion of these devices.

Videos of the devices were processed with computer vision tools from the OpenCV library relying on sparse optical flow to provide ways of consistently computing device speed and gaining insight into device operation for future designs.

First, a static image corresponding to the first frame was run through the Shi-Tomasi corner detection [39], to label points for future tracking. Across the analysis, 50 -100 points were used. Several points were tracked for reasons that will become clear in the mathematical analysis that follows. Moreover, individual points over a dense optical flow approach were tracked as in [12]. This reduced computational times and resulted in closer tracking of objects here, but could be useful with further tunning of the implementation.

The points idetified by the Shi-Tomasi algorithm were then fed to the Lukas-Kanade algorithm [27] for optical flow computations. Tracking was challenging, particularly since even during low-frequency motor operation, the motion of one step to the next occurs in less than $24\,\mathrm{ms}$ between camera frames. To somewhat improve this tracking, later generation devices have square etch-holes randomly interspersed troughout the rotor, such that the mass distribution is not significantly affected, but there are clear features for the computer and human
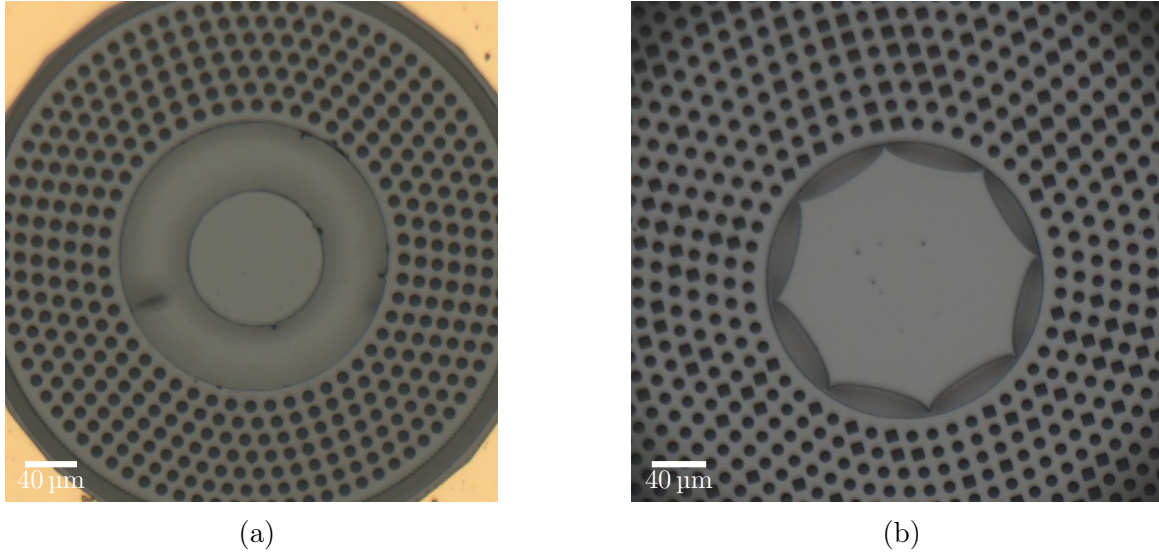
Figure 4.3: Etch holes used for motion tracking: (a) first generation, all-round uniform etch holes without top wafer cap; (b) improved etch hole pattern with random square etch holes, as seen through through wafer vias (cross section (c) in 3.3).

eye to track (as validation of tracking done here). This strategy is highly recommended for future MEMS implementations.

To understand the calculation of angular displacement and velocity, consider a rigid body that is translating and rotating in the image plane, as shown in Figure (4.4a).

For a given point B, the motion relative to an external frame of reference A can be computed as

$$\begin{aligned} \mathbf{v}_{B/A} &= \mathbf{v}_{B/O} - \mathbf{v}_{A/O} \\ &= \omega\hat{k} \times \mathbf{r}_{\mathbf{B/A}} \\ &= -\omega\, y_{B/A}\hat{i} + \omega\, x_{B/A}\hat{j} \end{aligned}$$

where the rotation vector $\omega\hat{k}$ is perpendicular to the plane of the image and $x_{B/A}, y_{B/A}$ are the relative position of point B with respect to point A. Moreover, this same velocity can be expressed in 2D, wtih u and v being the vertical and horizontal components of the velocity

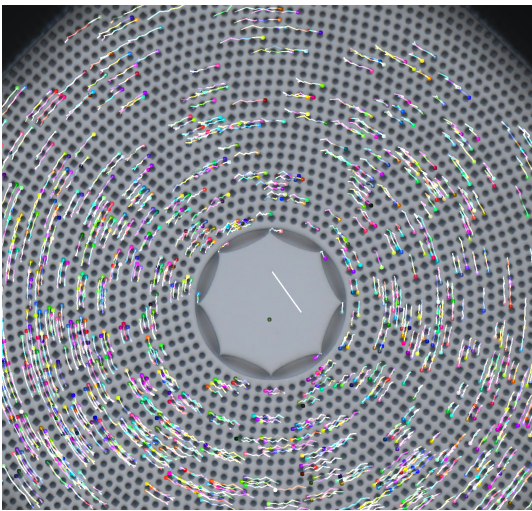$$\mathbf{v}_{B/A} = u_{B/A}\hat{i} + v_{B/A}\hat{j}.$$

Combining these two equations, there are two expressions for the angular rotation, ω

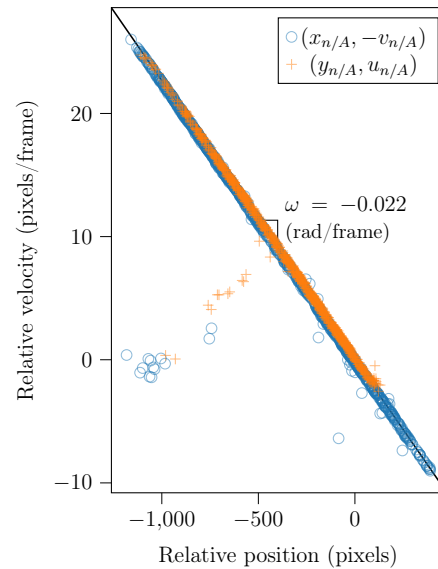$$\omega = -\frac{u}{y} \tag{4.7}$$

$$\omega = \frac{v}{x}, \tag{4.8}$$
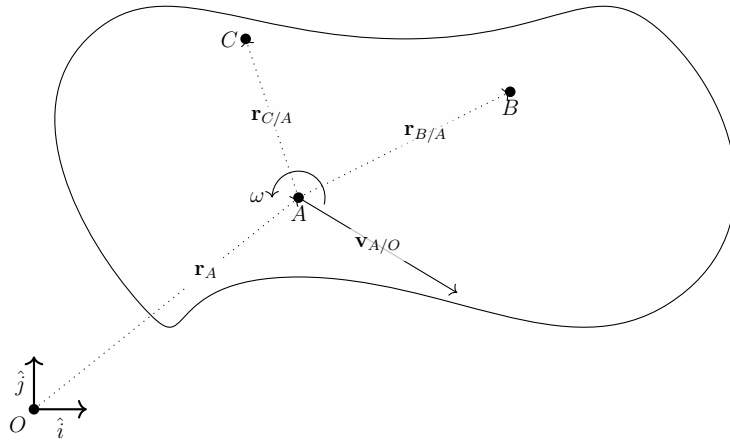
(a) Rigid body motion in 2D. We select point A on the body with velocity $\mathbf{v}_{A/O}$ relative to the origin. The angular velocity for the rigid body is ω and points B and C are sample points on the body.

(b) Example image tracking using Shi-Tomasi corner detection and Lukas-Kanade optical flow.

(c) Example computation of angular velocity from motion tracking data.

Figure 4.4: Motion tracking procedure.

with the subscript $_{B/A}$ ommited from u, v, x and y for clarity. Using these expressions for many points tracked in the system, the angular velocity ω can be calculated as the slope of the best-fit line of a scatter plot with points $(y_n, -u_n), (x_n, v_n)\}$ where n indexes all the points tracked. Figure (4.4c) shows an example of such a plot.

This methodology has two potential sources of errors. First, the Shi-Tomasi corner

detection algorithm can select corners that will not move with this rigid body. Because of the density of the etch holes, movable structures such as this rotor have a much higher density of corners that are deemed good to track by the algorithm. Therefore, most points being tracked are usually in the body of interest. Moreover, instead of performing a regular least-squares regression to compute angular velocity, the Random Sample Consensus (RANSAC) method was used, which fits the model excluding outliers.

The camera used for these videos had a pixel aspect ratio not equal to 1. In other words, vertical and horizontal pixels correspond to different lengths, so a correction factor found in the camera datasheet was applied.

One limitation in this setup is the frame rate of the camera, capped at 41.15 frames per second. This makes tracking faster rotation difficult, and manual tracking in the ImageJ software (FIJI distribution) had to be used to get values for higher speeds.

The remainder of this chapter focuses on the ways in which the collected data informed improvements to the design and conclussions on effective design choices.

4.2   Gold bonding and two-layer routing

One of the goals of the fabrication process was enabling two layer routing. For that, the structures presented in Figures (2.7) and (2.8) were designed.

Gold-Silicon contacts

For the first generation of these process, Boron-doped wafers with resistivity between 15 and $25\,\Omega\,\mathrm{cm}$ were used, which corresponds to around $10^{15}\,\mathrm{cm}^{-3}$ dopant density. Gold on silicon at these dopant densities does not produce an ohmic contact with linear I-V characteristics, but rather Shottky diodes with rectifying bahavior [7]. Figure (4.5) a shows rectifying behavior as the voltage is applied across the first (P1) and third terminal (P3), flowing through the bottom of the bridge test structure. Recall that in that design the bottom trace has a section of SOI only, meaning that current must flow across large metal-semiconductor junctions.

Moreover, these devices are known to act as photo-diodes, with current increasing with light intensity [7]. This explains why the leakage of current due to the bending of rectangular fingers in Figure (4.11) showed a dependence on the intensity of the microscope light. Additional complications arose during measurements, because the light intensity of this light source couples in 60 Hz noise from the power supply.

Beyond the rectifying behavior observed, it was also noted significant variations over repeated measurements of the same trace. The hypothesis is that this is the result of a breakdown that occurs when applying a range of -20 to 20 V.

This type of erratic behavior is not desirable for these devices, particularly if there is a need to draw conclusions from electrical observations alone. Thus, in the second generation wafers with an SOI layer resistivity $\rho < 0.01\,\Omega\,\mathrm{cm}$, or a dopant concentration of $10^{18}\,\mathrm{cm}^{-3}$ or larger were used. A higher dopant concentration reduces the Shottky barrier height and

results in an ohmic contact (see Chapter 3 in [44]). Figure (4.5b) shows the measurment of the I-V characterstics on bridge test structures with lower resistivity wafers. It was only possible to measure over a lower range of voltages because these reached the current limit of the devices. However, this was enough to validate the formation of ohmic contacts for the purposes of these motors.
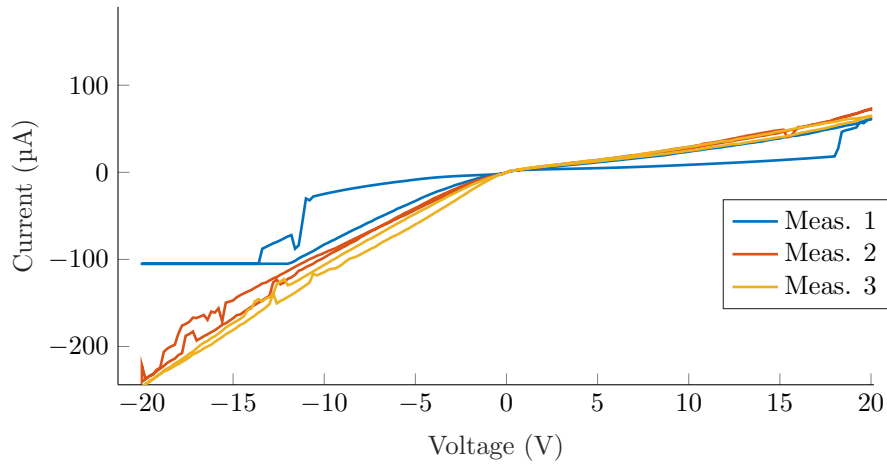
(a) First generation bridge, $\rho = 15 - 25\,\Omega\,\text{cm}$. Sequential measurments on the same bottom trace.
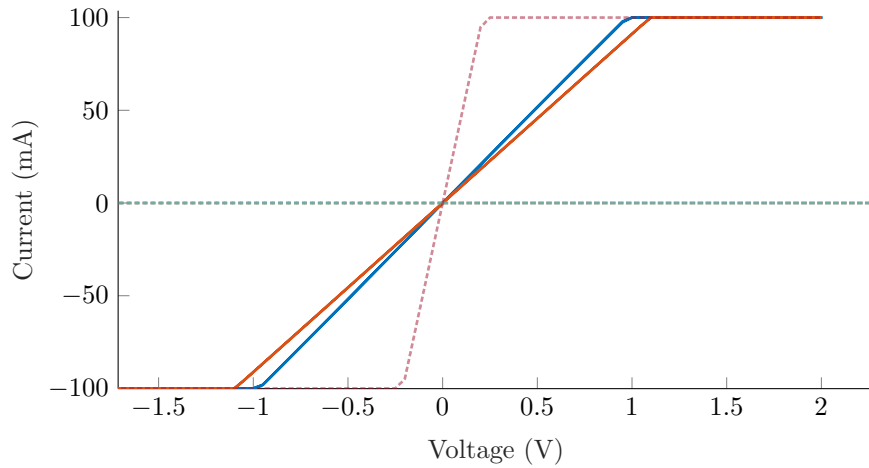
(b) Second generation bridge, including cross-trace resistances.

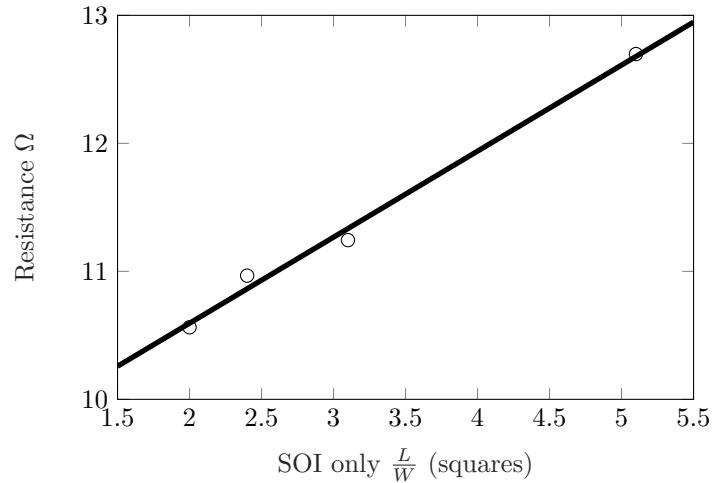Figure 4.5: I-V characteristics of bridge devices (Figure 2.7).

Figure 4.6: Bottom trace resistance versus SOI only dimensions. Fit line has a slope of $0.67\,\Omega/\square$.

Bridge structures

Recall from Section (2.3.2) that with the adition of the gold bonding process, there is an additional layer of routing. To validate this, an array of bridge structures was fabricated. The array had variation in the misalignment that would be tolerated between both traces from $50\,\mu$m to $200\,\mu$m. However, it was possible to achieve alignment better than $2\,\mu$m for wafer bonding and $18\,\mu$m for die bonding (Section (3.4.3)).

Figure (4.5) shows the I-V characteristics of a bridge test structure. The test structures worked as intended, as there is good connection through the top (from pad P1 to pad P3) and bottom traces (P2-P4), but very high resistance between all other terminals. With this measurement setup, there is a $2.1\,\Omega$ resistance when probing the same pad. Crucially, there is no shorting between the top and bottom traces, meaning in these motors, the signals are kept distinct.

Furthermore, plotting the varying resistance as the dimensions of the non-metalized portion of SOI vary. Fitting the data to the measurments by approximating the neck with a length and width, a resistivity of $0.67\,\Omega/\square$ was observed, which corresponds to $0.0027\,\Omega$ cm, following the specification for wafers below $0.01\,\Omega$ cm. In the context of these devices, the internal resistances contributed by the Au-Si contact and the SOI layer remain low.

Contact resistance

Structures to perform 4-wire measurments of the contact resistance were also designed, such as Figure (2.8). The contact resistance of squares was measured to range from $50\,\mu$m on a side to $400\,\mu$m on a side.

Figure (4.7) shows 4 point measurments of contact resistance after bonding. The resistance is not in an inverse relationship with the area, but this is to be expected since all resistances are below $5\,\text{m}\Omega$. Smaller versions of theses structures should always be included in fabrication processes with gold-gold bonding, so that the quality of the bond can be assessed from an electrical perspective.
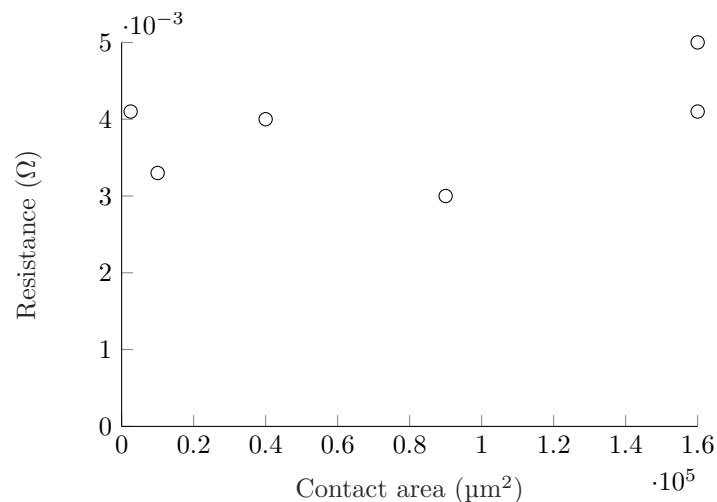

Figure 4.7: 4-point measurement of contact resistance as a function of contact area.

Bond strength

When bonding was unsuccesful, this became quickly apparent during handling. The strength of two bonded chips under tensile stress was also measured. A nut was carefully epoxied on both sides of a bonded chip with a metal contact area of $2.018 \times 10^{-5}\,\text{m}^2$, as shown in Figure (4.8). Then bolts were screwed onto the nuts and tensile force was applied witha Mark-10 force gauge, measuring the maximum stress before failure at 22.7 N and 39.6 N, which correspond to $1.12\,\text{MPa}$ and $1.96\,\text{MPa}$.The tested chips were bonded at a wafer level, with an applied pressure of $30\,\text{MPa}$.

4.3 Motor performance in dry conditions

4.3.1 First generation motors

First-generation motors served as proof-of-concept. As a first step, it was noted that the devices that underwent all the fabrication processes except releasing were functional. The pairing of video data with electrical data provided insight into several necessary improvements.
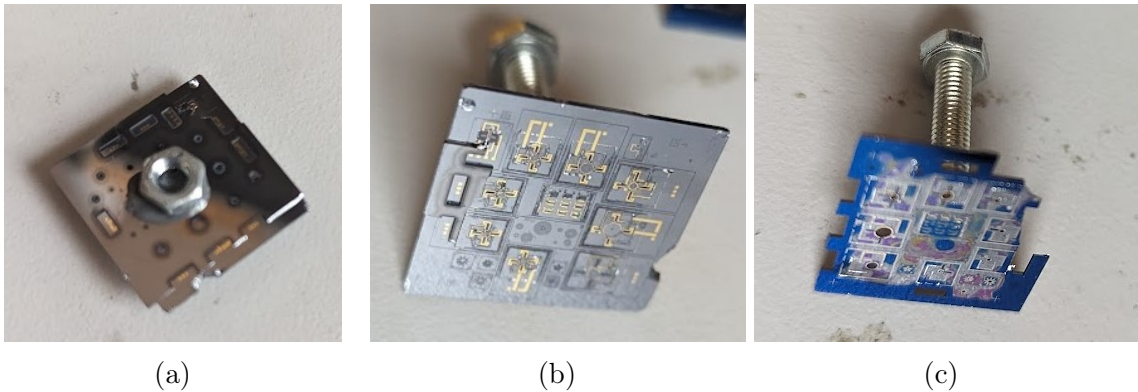
(a)   (b)   (c)

Figure 4.8: Bonding strenght test: Chip is epoxied to 2 nuts (a), and tested until it reaches tensile failure. After failure, images of both sustrate (b) and lid (c) are observed.

First functional motor

Initially after fabrication without the lid, none of devices 1A, 1B, and 1C were functional, although the gap-closers actuating followed the designed. For device 1A, the shuttle was not attached in any way to the rotor and was lost after release. For devices 1B and 1C, the 1-spring hub led to asymetry in forces. Careful observation of the videos shows that the shuttle after 1 rotation the shuttle displaced in x and y such that only 2 pawls (north and east) made contact with the shuttle. As discussed in Chapter (2), in future designs the 1-spring shuttle was deprecated.

It was possible to carefully break the spring on device 1B and show the first rotational steps of the micromotors. Extensive testing and careful analysis of the video data of this first functional device led to significant improvements.

Figure (4.9) shows the tracking of an uncapped, first generation device, and Figure (4.10) shows the result of tracking the motion in the shuttle and both sets of GCA-A and GCA-B. Data for GCA-A actuation (North/South) is unrealiable because it was not possible capture all 4 pawls with sufficient resolution with the camera equipment available.

There are aspects of the design that worked as expected. When closing the gaps, the GCAs moved 4.8 µm, precisely $g_1 - g_s$ as designed (Table 2.1.) Moreover, the rotational steps occur exactly when either one of the sets of pawls re-engages with the shuttle.

Qualitatively, the motion produced is clunky: the motor does not take steps at regular intervals. Moreover, at the voltages used (50 V), the left GCA does not close completely, as seen in Figure (4.9). The hypothesis was that this occurs because the shuttle shifted off-center. Careful analysis of the third and fourth plots in Figure (4.10) reveals the West GCA-B engages when GCA-A shifts the shuttle's position. Of particular importance here, there is significant wobble room on the central shuttle: it displaces up to 3 µm in the x direction during actuation. When the shuttle shifts, there is uneven loading of the motors and skipped steps. To mitigate translation shuttle shifts, designs with much tighter tolerances to a central
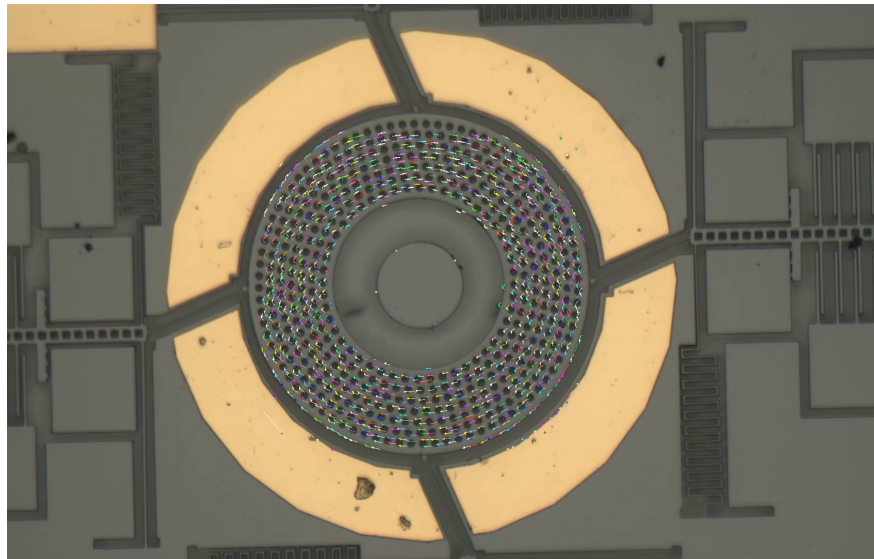
Figure 4.9: Rotation of first-generation motor: we show tracking of the central shuttle. Motion was also track on GCA-A (South) and GCA-B(East and West) as shown in Figure 4.10. The snapshot corresponds to t=0.36 s. Devices tested without wafer bonding for assesment of operation.

rotor were introduced, as described in Chapter 2.

Leakage currents in GCAs

The rectangular fingers in a variable capacitor can bend under force. Although these devices were designed to avoid shorting due to the bending of capacitor fingers by the electrostatic force up to 120 V. However, high leakage currents were observed during testing. Figure (4.11) shows the current for a device as the voltage supplied V_{DD} was increased. From the video data, pull-in ocurred for these devices above 47.5 V. For voltages between 47.5 V and 67.5 V, the current spike for charging drops down to zero eventually.

However, voltages above 67.5 V resulted in the current plateauing until the GCAs were disengaged. This is likely the result of the fingers in the capacitor bending and providing a path for current to short. Overetch during DRIE beyond what is budgeted could exacerbate the issue. During operation, high leakage currents would greatly increase power consumption and be undesirable.

Interestingly, a dependency between the maginitude of leakage currents and the light shone on the device was noted. Although the light intensity was not measured or accurately controlled, there is a trend that demonstrates the complete resistance path depends on light intensity. This is likely the result if photocurrents in Au-Si Schottky junctions dicussed in Section (4.2).
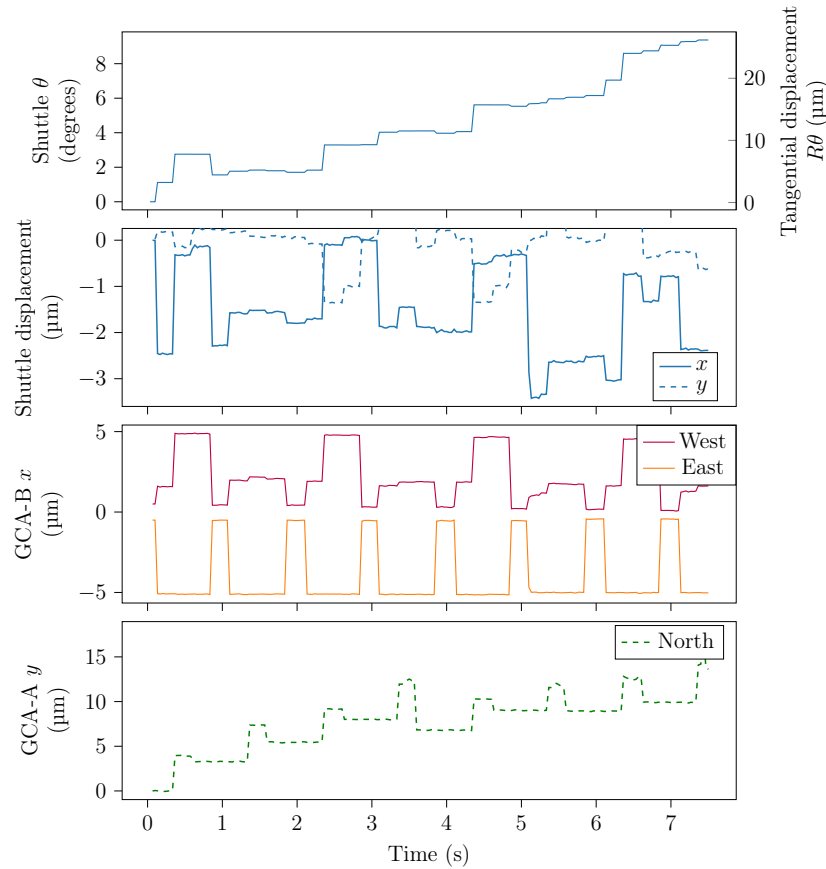
Figure 4.10: Motion of shuttle and GCA motion for motor 1A with a broken spring at 1 Hz.
Top: shuttle rotation as a function of time
Second: x and y positions of the shuttle with respect to the starting location.
Third:x displacement during actuation of GCA-B.
Bottom: single GCA-A actuating. Drift in position is a unwanted result of tracking at the
edge of the image.

4.3.2   Second generation devices

In the second generation of devices, functional devices in a wide range of conditions were
measured. All second generation fabrication produced bonded devices (Figure 3.3c), there
is limited data on pawl synchronicity with the steps.

For the experiments shown in Figure 4.12, $t_1 = 100\,\mu s$, (as defined in Figure (2.2).This
means that the device should take a step every $200\,\mu s$, so a full cycle of the motor are running
at $2.5\,Hz$).

Figure (4.12) shows discrete steps of motor 2B, which has a radius of $300\,\mu m$. The
device has a convex hub, which reduces the issues observed in first-generation devices with
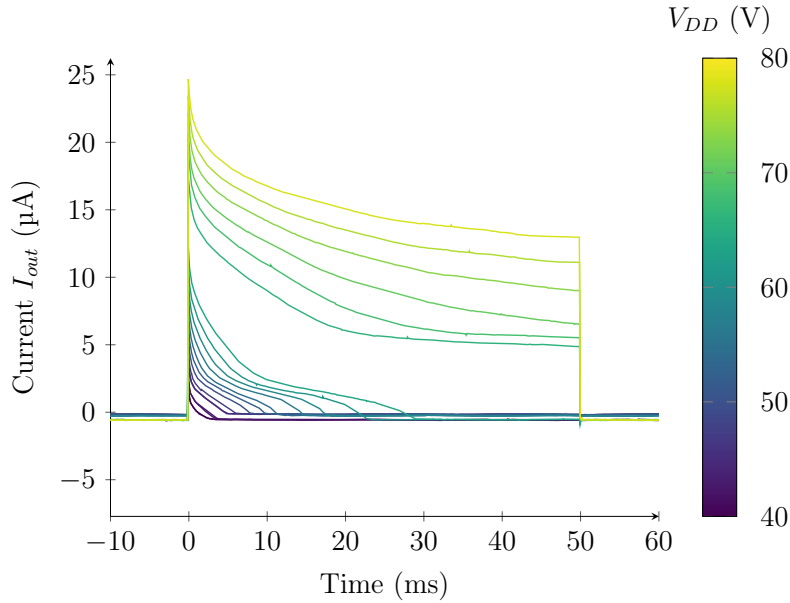
(a) Charging current at full light
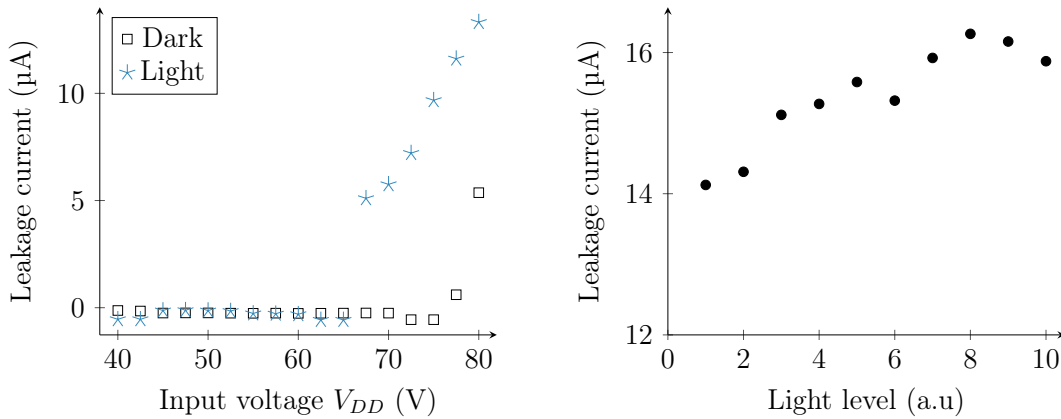
(b) Leakage current for different input voltages V_{DD}

(c) Leakage currents at 80 Volts over varying light

Figure 4.11: Current due to finger bending. In these experiments, pull in happened above 47 V. Leakage current is defined as the current value once it plateus.

translation of the shuttle. This results in more consistent, but not perfect, steps. The device is actuated with $t_1 = 100$ ms as defined in Figure (2.2). This means the device should take a step every 200 µs, which aligns with the observed values. Steps range from 1 to 5 µm at the point of contact with the shuttle. It is possible this variation in step size is due to imperfect

alignment between the shuttle teeth and the pawl teeth. For larger voltages, the likelyhood of moving the shuttle "over the hump" for the next tooth increases, as the force delivered to the shuttle is larger. Notice as well that at 30 V, the GCAs did not produce any motion, because the voltage is not high enough for pull-in.
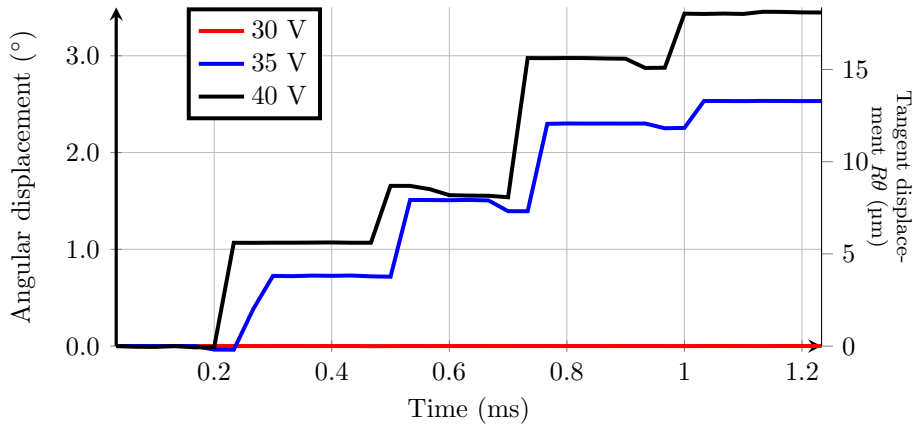
Figure 4.12: Discrete steps of device 2B($R_{shuttle} = 300\,\mathrm{\mu m}$) at voltages below and above pull in.
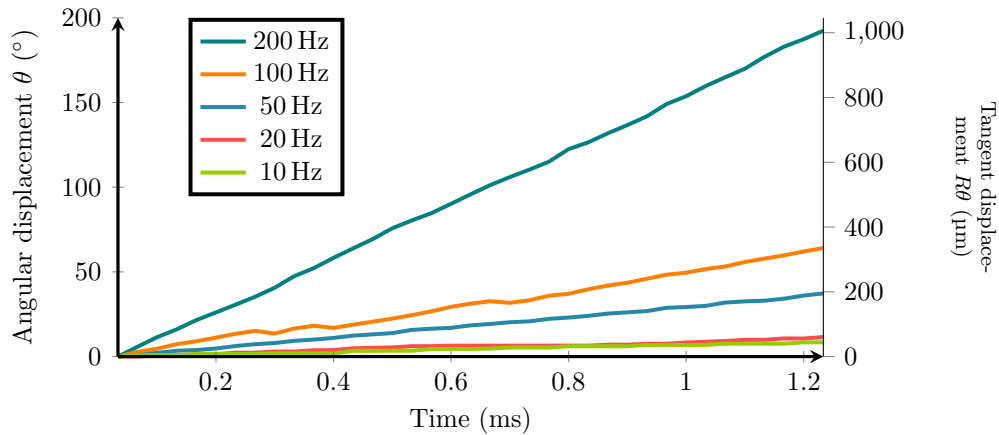
Figure 4.13: Velocity at different actuation frequencies for device 2B ($R_{shuttle} = 300\,\mathrm{\mu m}$) at 40 V actuation.

With the camera equipment available, limited to 42.15 fps, the details seen at low frequencies get averaged out as the actuation frequency is averaged. Figure (4.13) shows angular displacement for the same device (2B). As expected, the velocity increases as actuation frequency increases. At 200 Hz, the average is $4\,\mathrm{\mu m}$ per cycle ($2\,\mathrm{\mu m}$ per step).

(a) Linear   (b) Logarithmic scale
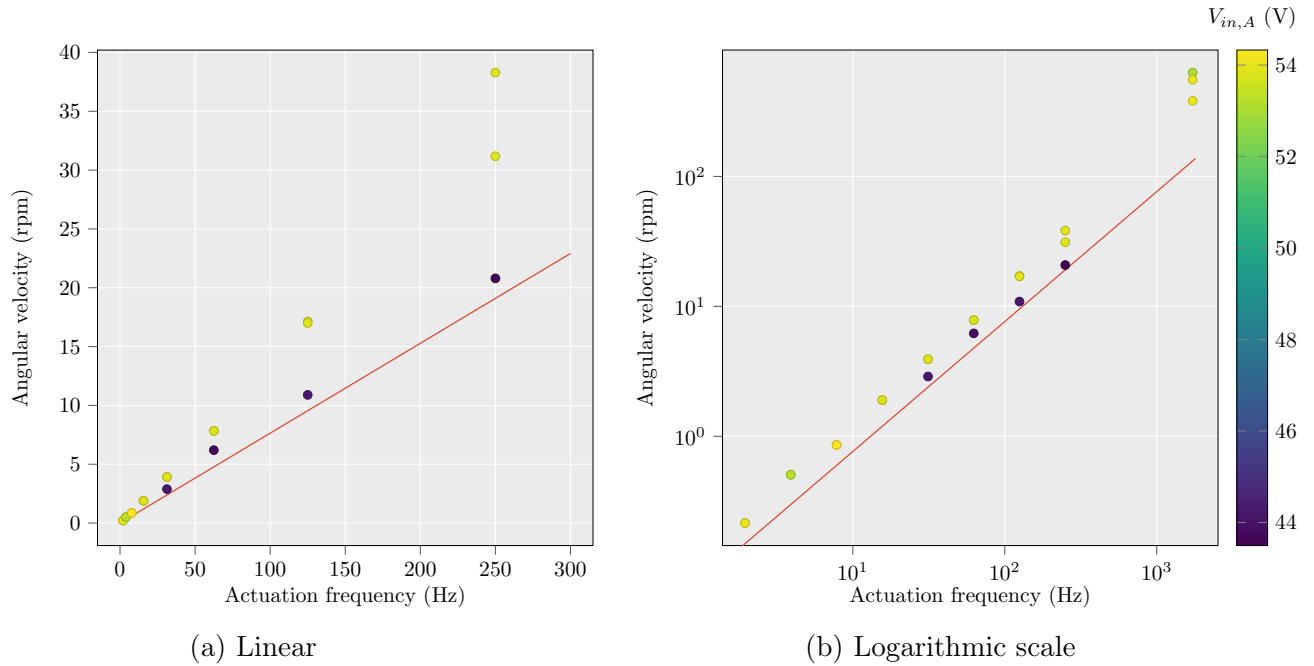
Figure 4.14: Speed of rotary motor 2C based on motor frequency. The red line shows the projected speed for a motor that moves 4 μm per cycle. We plot in a logarithmic scale to more accurately visualize the higher frequency actuation.

Figure (4.14) shows the velocities for our best performing device. The results match are colored by the amplitude of $V_{in,A}$, the input voltage to the device as measured. At lower input voltages, the speed matches the design intent: every cycle of the motor the shuttle rotates over $s_t = 4$ μm, the pitch between teeth in the shuttle.

For higher voltages, speeds are slightly higher. As found by Contreras [9] on linear inchworm motors with similar characteristics, the inertia of the shuttle is responsible for these higher speeds. However, in the inteded operation case with a flagellum this phenomenon would not show. The highest frequencies of operation were 1.66 kHz, which resulted in maximum velocities observed of 633 rpm. This is above the range set out as a goal for a 500 μm radius shuttle in Chapter (1). However, the introduction of viscous forces on the shuttle would definitely slow it down or require higher voltages to overcome these forces in the flagellum. Regardless, we have demonstrated the capacity to operate a high frequencies. It should be noted that at such high frequencies, we observe somewhat erratic behavior. For example, the motor would rotate very quickly for a few seconds, and then completely stop for another few seconds. A high speed camera correctly triggered with the electrical signals that is designed for microscopic use would provide more insight.

These experiments were conducted with a large resistive load of $R_{meas} = 4.65$ MΩ, the charging time constants are around 6 μs. Therefore, we are also approching the limit of of

how fast we can charge and discharge the capacitors. However, a lower resistance circuit could potentially drive the motors up to our projected maximum frequency.

Finally, we were able to integrate the power at 54 V using oscilloscope data collected for a total power of 380 pJ/cycle.

Force estimation

We were able to use device 2D, with a 2-spring hub to estimate the force delivered by the motors at the pawl. When the device was actuated at 7.5 kHz using only one set of pawls, we observed back and forth with an amplitude of 0.024°. We used the model in [9], and treat the serpentine springs as clamped-guided flexures in parallel. With this, we have a rotational constant

$$k_\theta = k_s R^2 = 1.28\,\text{µNm/rad},$$

where R is the radius at which the springs attach to the shuttle. This results in a maximum torque measured of 561 pN m at 40 volts (equivalent to 749 nN applied by the pawls on the edge of the shuttle). For comparison, the GCAs in device 2D should be around 1.47 mN. It should be noticed that this measurement is based on a single estimation with small deflectance, which could be hard for our cameras and motion tracking system to accurately detect. For future work with rotational springs, using much more compliant springs and larger capacticance GCAs would result in higher displacements that can be accurately tracked.
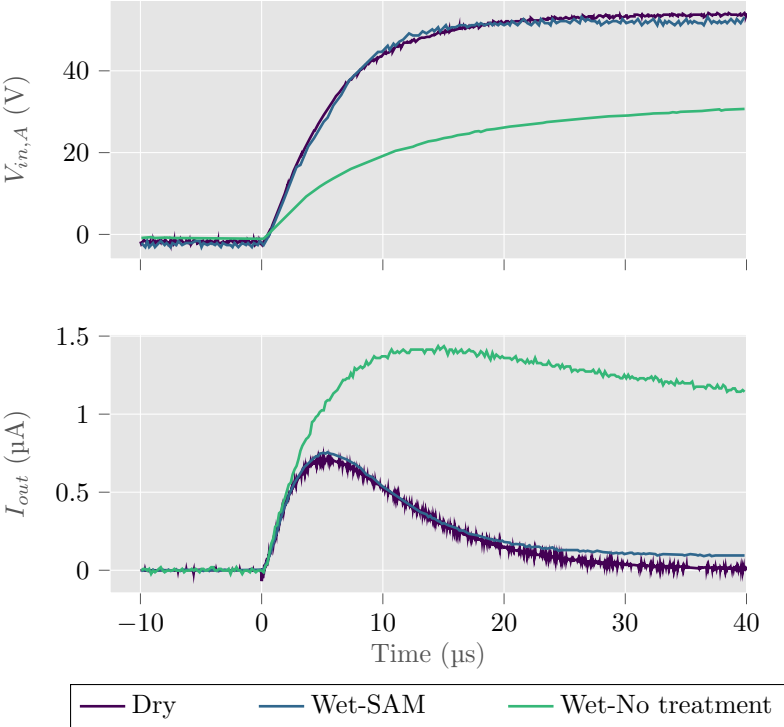
(a) GCA charging waveforms
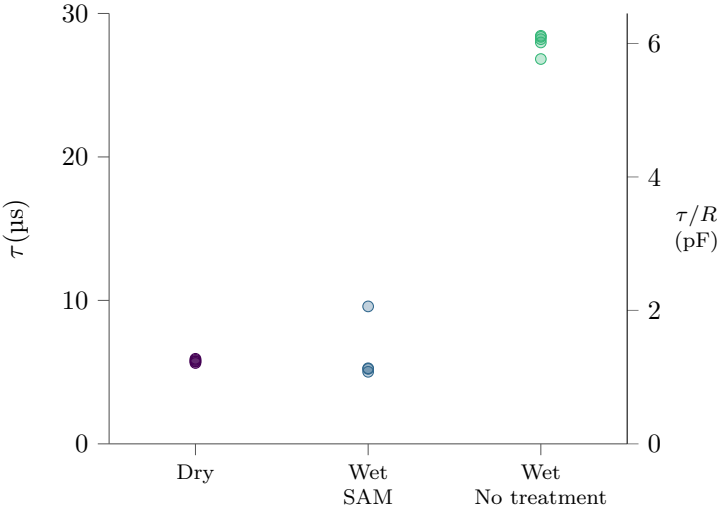
(b) Charging time constant

Figure 4.15: Charging of a GCA, with $V_{DD} = 50$V for three conditions: Dry devices (2C), wet devices with applied hydrophobic SAM, and wet devices without surface treatment.

4.4 Underwater operation

4.4.1 Electrical evidence of hermetic packaging

One of the goals of this invistigation was to progresss toward motors that can operate underwater. As of this writing, spinning of the rotor underwater was not achieved. However, we have experimental results that show water ingress into the GCA area was prevented by the design with small gaps and a hydrophobic self-assembled monolayer (SAM) applied on the surface.

Figure (4.15) shows the charging voltage and current waveforms for a device under three distinct conditions. First, the motor was operated normally under dry conditions. Then, water is added on top of the through wafer via of that same device, which had a SAM treatment for hydrophobicity. We compare this to a motor that was not treated, and therefore had contact angles below 90 °. The third, untreated device, shows significant deviation in its electrical characteristics when submerged in water. Faradaic currents were found as there was a significant increase in the current and the voltage across the device is limited.

The time constant was computed with least-squares method and used to estimate capacitance as $C \approx \tau/R_{meas}$. Note that the capacitance estimated with this method lies between the expected open and closed capacitances for motor 2C (Table 2.3). However, in the device with clear water ingress, capacitance increases because of the higher dielectric constant of water. With a hydrophobic coating, the Laplace pressure prevents liquid ingress to the GCA area. Therefore, we see no significant change in capacitance, approximated as $C = \tau/R_{meas}$ in Figure 4.15.

We do not have conclussive evidence on why effective rotation underwater was no achieved. However, we can hypothesize probable causes. During rotation surface tension acts in a radial, rather than tangential direction. However, the presence of corners and gaps in the device can create surface forces that prevent the shuttle from rotating. Another possible failure mechanism is the sticking of the pawl to the shuttle, pinned by air water interfaces. Thus, although the GCAs actuate successfuly, the angled arm is not able to disengage in order to take the next step. There is also a possibility that the pressure of the water pushes the shuttle down and increases friction between the shuttle and the substrate beyond the forces designed by our devices.

4.4.2 Final thoughts and future work

This dissertation details the motivation, design, and fabrication of an electrostatic rotational motor. It describes a 2-wafer, 4-mask process that enables two-layer routing and hermetic packaging in aqueous environments.

A motor capable of rotations up to 633 rpm was built and demonstrated, with solutions addressing high leakage currents and earlier design flaws. Moreover, the process developed here allows for through-wafer, out-of-plane vias. MEMS designs are often constrained to the

in-plane dimension, but the techniques used here can be applied to more effectively build out-of-plane devices.

To achieve true underwater operation, several strategies could be considered. First, devices with uniform gaps should be designed: corners and small variable gaps can result in high surface forces that pin structures and prevent them from moving. Additionally, for a design like ours, the difference in diameter between the through-wafer via and the rotational shuttle should be increased. A continuous air-water interface at the rotor would not oppose rotation, whereas moisture at the pawls can result in sticking of devices. Moreover, devices with a higher force output can be designed to test whether failure to rotate is only the result of underestimating the necessary torque.

Another interesting possibility is to flood the GCAs with oil before submerging the devices in water. If air-water interfaces are effectively avoided, surface tension cannot result in the sticking of components.

Furthermore, the process described in this dissertation can be used for a completely different type of device, such as those that need to interact with the environment. Using Laplace pressure to our advantage can be a powerful packaging technique. To be clear, air-water interfaces do not prevent the diffusion of water molecules in vapor form. However, protection of electrostatic MEMS without bulky packaging is indeed beneficial.

This work addresses a small subset of the problems required for an effective and controllable propulsion mechanism. However, there is still a long way to go in creating truly autonomous microswimmers.

Bibliography

[1] C David Andereck, SS Liu, and Harry L Swinney. "Flow regimes in a circular Couette system with independently rotating cylinders". In: *Journal of fluid mechanics* 164 (1986), pp. 155–183.

[2] Roberto Bernasconi et al. "Fabrication of Bioinspired Artificial Bacterial Flagella Via Two Photon Lithography and Wet Metallization". In: *2021 21st International Conference on Solid-State Sensors, Actuators and Microsystems (Transducers)*. IEEE. 2021, pp. 369–372.

[3] Nicolas Bertin et al. "Propulsion of bubble-based acoustic microswimmers". In: *Physical Review Applied* 4.6 (2015), p. 064012.

[4] Bram Bet et al. "Efficient shapes for microswimming: From three-body swimmers to helical flagella". In: *The Journal of chemical physics* 146.8 (2017).

[5] Ada-Ioana Bunea and Rafael Taboryski. "Recent advances in microswimmers for biomedical applications". In: *Micromachines* 11.12 (2020), p. 1048.

[6] Mathilde Callies et al. "Microfabricated textured surfaces for super-hydrophobicity investigations". In: *Microelectronic engineering* 78 (2005), pp. 100–105.

[7] TP Chen et al. "Current transport and its effect on the determination of the Schottky-barrier height in a typical system: Gold on silicon". In: *Solid-state electronics* 36.7 (1993), pp. 949–954.

[8] Daniel S Contreras and Kristofer SJ Pister. "Dynamics of electrostatic inchworm motors for silicon microrobots". In: *2017 International Conference on Manipulation, Automation and Robotics at Small Scales (MARSS)*. IEEE. 2017, pp. 1–6.

[9] Daniel Savino Contreras. *Walking silicon: Actuators and legs for small-scale terrestrial robots*. eScholarship, University of California, 2018.

[10] Mehmet Akif Erismis et al. "A water-tight packaging of MEMS electrostatic actuators for biomedical applications". In: *Microsystem technologies* 16 (2010), pp. 2109–2113.

[11] Rouhollah D Farahani, Kambiz Chizari, and Daniel Therriault. "Three-dimensional printing of freeform helical microstructures: a review". In: *Nanoscale* 6.18 (2014), pp. 10470–10485.

[12] Gunnar Farnebäck. "Two-frame motion estimation based on polynomial expansion". In: *Image Analysis: 13th Scandinavian Conference, SCIA 2003 Halmstad, Sweden, June 29–July 2, 2003 Proceedings 13*. Springer. 2003, pp. 363–370.

[13] Richard P Feynman. "Plenty of Room at the Bottom". In: *APS annual meeting*. 1959.

[14] Tianjiao Gong et al. "Investigation of Vapor HF Sacrificial Etching Characteristics Through Submicron Release Holes for Wafer-Level Vacuum Packaging Based on Silicon Migration Seal". In: *Journal of Microelectromechanical Systems* (2023).

[15] James Gray and Gregory J Hancock. "The propulsion of sea-urchin spermatozoa". In: *Journal of Experimental Biology* 32.4 (1955), pp. 802–814.

[16] Yingzheng He et al. "Bubble-based Microrobot: Recent Progress and Future Perspective". In: *Sensors and Actuators A: Physical* (2023), p. 114567.

[17] Cari F Herrmann et al. "Conformal hydrophobic coatings prepared using atomic layer deposition seed layers and non-chlorinated hydrophobic precursors". In: *Journal of Micromechanics and Microengineering* 15.5 (2005), p. 984.

[18] Gilgueng Hwang et al. "Manufacturing of 3D Helical Microswimmer by AFM Micromanipulation for Microfluidic Applications". In: *IEEE Transactions on Semiconductor Manufacturing* 34.3 (2021), pp. 248–255.

[19] Jasmine Jan et al. "Flexible Blade-Coated Optoelectronic Devices: Dual Functionality via Simultaneous Deposition". In: *Advanced Functional Materials* 32.25 (2022), p. 2112343.

[20] Mustaphis Koleoso et al. "Micro/nanoscale magnetic robots for biomedical applications". In: *Materials Today Bio* 8 (2020), p. 100085.

[21] Takaaki Kurinomaru et al. "Protein microswimmers capable of delivering cells for tissue engineering applications". In: *Materials Horizons* 7.3 (2020), pp. 877–884.

[22] Pierre Lambert et al. "Surface tension in microsystems". In: *Engineering Below the Capillary Length* (2013).

[23] Jong Hyun Lee et al. "Characterization of anhydrous HF gas-phase etching with CH3OH for sacrificial oxide removal". In: *Sensors and Actuators A: Physical* 64.1 (1998), pp. 27–32.

[24] David Leith. "Drag on nonspherical objects". In: *Aerosol science and technology* 6.2 (1987), pp. 153–161.

[25] Yanqiao Li, Benjamin L Dobbins, and Jason T Stauth. "An 80-117V Pseudo-Adiabatic Drive Circuit for Microrobotic Actuators with Optical Power Delivery and Peak Power Reduction Factor over 14×". In: *2020 IEEE Custom Integrated Circuits Conference (CICC)*. IEEE. 2020, pp. 1–4.

[26] Lisheng Liu et al. "How to make a fast, efficient bubble-driven micromotor: A mechanical view". In: *Micromachines* 8.9 (2017), p. 267.

[27] Bruce D Lucas and Takeo Kanade. "An iterative image registration technique with an application to stereo vision". In: *IJCAI'81: 7th international joint conference on Artificial intelligence*. Vol. 2. 1981, pp. 674–679.

[28] Alex Moreno et al. "Single-chip micro-mote for microrobotic platforms". In: *Government Microcircuit Applications & Critical Technology Conference. GOMACTech*. 2020.

[29] Samantha Norris et al. "Optically-Powered Microscopic Bubble Rockets". In: *APS March Meeting Abstracts*. Vol. 2021. 2021, R24–009.

[30] Aaron T Ohta et al. "Optically actuated thermocapillary movement of gas bubbles on an absorbing substrate". In: *Applied physics letters* 91.7 (2007).

[31] Stefano Palagi et al. "Structured light enables biomimetic swimming and versatile locomotion of photoresponsive soft microrobots". In: *Nature materials* 15.6 (2016), pp. 647–653.

[32] I Penskiy and S Bergbreiter. "Optimized electrostatic inchworm motors using a flexible driving arm". In: *Journal of Micromechanics and Microengineering* 23.1 (2012), p. 015018.

[33] Edward M Purcell. "Life at low Reynolds number". In: *American journal of physics* 45.1 (1977), pp. 3–11.

[34] Famin Qiu et al. "Artificial bacterial flagella functionalized with temperature-sensitive liposomes for controlled release". In: *Sensors and Actuators B: Chemical* 196 (2014), pp. 676–681.

[35] Jan S Rentmeister et al. "A 120–330V, Sub-μA, 4-Channel Driver for Microrobotic Actuators with Wireless-Optical Power Delivery and over 99% Current Efficiency". In: *2020 IEEE Symposium on VLSI Circuits*. IEEE. 2020, pp. 1–2.

[36] Bruce Rodenborn et al. "Propulsion of microorganisms by a helical flagellum". In: *Proceedings of the National Academy of Sciences* 110.5 (2013), E338–E347.

[37] Ethan Schaler et al. "SWIM-Sensing with Independent Micro-swimmers". In: *The Astrobiology Science Conference (AbSciCon) 2022*. 2022, pp. 417–05.

[38] Craig B Schindler et al. "A jumping silicon microrobot with electrostatic inchworm motors and energy storing substrate springs". In: *2019 20th International Conference on Solid-State Sensors, Actuators and Microsystems & Eurosensors XXXIII (TRANSDUCERS & EUROSENSORS XXXIII)*. IEEE. 2019, pp. 88–91.

[39] Jianbo Shi et al. "Good features to track". In: *1994 Proceedings of IEEE conference on computer vision and pattern recognition*. IEEE. 1994, pp. 593–600.

[40] Ryan M Shih et al. "Characterization of electrostatic gap-closing actuator arrays in aqueous conditions". In: *2018 IEEE Micro Electro Mechanical Systems (MEMS)*. IEEE. 2018, pp. 596–599.

[41] Soner Sonmezoglu et al. "A method and analysis to enable efficient piezoelectric transducer-based ultrasonic power and data links for miniaturized implantable medical devices". In: *IEEE Transactions on Ultrasonics, Ferroelectrics, and Frequency Control* 68.11 (2021), pp. 3362–3370.

[42] Thomas L Sounart, Terry A Michalske, and Kevin R Zavadil. "Frequency-dependent electrostatic actuation in microfluidic MEMS". In: *Journal of Microelectromechanical Systems* 14.1 (2005), pp. 125–133.

[43] Yoshiyuki Sowa and Richard M Berry. "Bacterial flagellar motor". In: *Quarterly reviews of biophysics* 41.2 (2008), pp. 103–132.

[44] Simon M Sze, Yiming Li, and Kwok K Ng. *Physics of semiconductor devices*. John wiley & sons, 2021.

[45] S Tajima and K Komvopoulos. "Physicochemical properties and morphology of fluorocarbon films synthesized on crosslinked polyethylene by capacitively coupled octafluorocyclobutane plasma". In: *The Journal of Physical Chemistry C* 111.11 (2007), pp. 4358–4367.

[46] Christine H Tsau. "Fabrication and characterization of wafer-level gold thermocompression bonding". PhD thesis. Massachusetts Institute of Technology, 2003.

[47] Ruoxuan Wu et al. "Recent Process in Microrobots: From Propulsion to Swarming for Biomedical Applications". In: *Micromachines* 13.9 (2022), p. 1473.

[48] Li Zhang et al. "Artificial bacterial flagella: Fabrication and magnetic control". In: *Applied Physics Letters* 94.6 (2009).

Appendix A

Accompanying code

This appendix contains links to the code used for this work. There are two main repositories.

Layout and Design

`https://mauribusta@bitbucket.org/mauribusta/rotary_inchworm.git` The repository here includes the code to analyze and optimize the design, as well as layout using the gdspy libary.

Motion tracking and analysis

`https://github.com/PisterLab/flagellar_motor.git` This repository contains the code used for analysis of videos, motion tracking, and the combination of electrical and video performance.